



**DEVELOPMENT OF EFFICIENT ALGORITHMS FOR FLICKER,
HARMONICS AND INTERHARMONICS ESTIMATIONS AND POWER
QUALITY EVENT CLASSIFICATION SPECIALLY DESIGNED FOR
HIGHLY TIME-VARYING LOADS OF POWER SYSTEMS**

**A THESIS SUBMITTED TO
THE GRADUATE SCHOOL OF NATURAL AND APPLIED SCIENCES
OF
GAZİ UNIVERSITY**

**BY
Ebrahim BALOUJI**

**IN PARTIAL FULFILLMENT OF THE REQUIREMENTS
FOR
DOCTOR OF PHILOSOPHY IN
ELECTRICAL ELECTRONICS ENGINEERING**

July 2019

The thesis study titled "DEVELOPMENT OF EFFICIENT ALGORITHMS FOR FLICKER, HARMONICS AND INTERHARMONICS ESTIMATIONS AND POWER QUALITY EVENT CLASSIFICATION SPECIALLY DESIGNED FOR HIGHLY TIME-VARYING LOADS OF POWER SYSTEMS" is submitted by Ebrahim BALOUJI in partial fulfillment of the requirements for the degree of Doctor of Philosophy in the Department of Electrical Electronics Engineering, Gazi University by the following committee.

Supervisor: Prof. Dr. Özgül SALOR DURNA

Electrical Electronics Engineering, Gazi University

I certify that this thesis is a Doctor of Philosophy thesis in terms of quality and content

Chairman: Prof. Dr. Muammer ERMİŞ

Electrical Electronics Engineering, Middle East Technical University

I certify that this thesis is a Doctor of Philosophy thesis in terms of quality and content

Member: Prof. Dr. Timur AYDEMİR

Electrical Electronics Engineering, Gazi University

I certify that this thesis is a Doctor of Philosophy thesis in terms of quality and content

Member: Prof. Dr. Işık ÇADIRCI

Electrical Electronics Engineering, Hacettepe University

I certify that this thesis is a Doctor of Philosophy thesis in terms of quality and content

Member: Assoc. Prof. Dr. Hasan Şakir BİLGE

Electrical Electronics Engineering, Gazi University

I certify that this thesis is a Doctor of Philosophy thesis in terms of quality and content

Date: 03/07/2019

I certify that this thesis, accepted by the committee, meets the requirements for being a Doctor of Philosophy Thesis.

.....

Prof. Dr. Sena YAŞYERLİ

Dean of Graduate School of Natural and Applied Sciences

Fen Bilimleri Enstitüsü Müdürü

ETHICAL STATEMENT

I hereby declare that in this thesis study I prepared in accordance with thesis writing rules of Gazi University Graduate School of Natural and Applied Sciences;

- All data, information and documents presented in this thesis have been obtained within the scope of academic rules and ethical conduct,
 - All information, documents, assessments and results have been presented in accordance with scientific ethical conduct and moral rules,
 - All material used in this thesis that are not original to this work have been fully cited and referenced,
 - No change has been made in the data used,
 - The work presented in this thesis is original,
- or else, I admit all loss of rights to be incurred against me.

Ebrahim BALOUJI

03/07/2019

**GÜÇ SİSTEMLERİNİN ZAMANDA HIZLI DEĞİŞEN YÜKLERİ İÇİN ÖZEL
TASARLANMIŞ KIRPIŞMA, HARMONİK VE ARAHARMONİK KESTİRİMİ VE
GÜÇ KALİTESİ OLAY SINIFLANDIRMASI İÇİN VERİMLİ ALGORİTMALARIN
GELİŞTİRİLMESİ**

(Doktora Tezi)

Ebrahim BALOUJİ

GAZİ ÜNİVERSİTESİ
FEN BİLİMLERİ ENSTİTÜSÜ

Haziran 2019

ÖZET

Bu tezin amacı, akıllı bir güç kalitesi (GK) çözümleme sistemi oluşturmak için gerekli tamamlayıcı araçları geliştirmektir. Güncel bilimsel yazın ve ticari GK ölçüm cihazları incelendiğinde şu üç gereksinim ortaya çıkmıştır: kırpışma tespiti için hafıza ve işlem açısından verimli algoritma ihtiyacı, zamanda değişen harmonik ve araharmoniklerin tespiti için gerçek-zamanlı algoritmalar ve yüksek doğrulukta GK olay tespiti. İlk olarak, kırpışmayı tahmin etmek için, gerilim dalga biçiminin yerine girdi olarak gerilim dalga biçiminin kök ortalama karesini (RMS) kullanarak IEC'nin (Uluslararası Elektroteknik Komite) kırpışma-ölçer standardında önerilen ölçüm yönteminin sayısal olarak gerçekleştirilmesi sunulmaktadır. Amaç, sadece gerilim dalga formunun RMS değerleri mevcut olduğunda, IEC kırpışma-ölçer standardı IEC 61000-4-15'e göre titreşim şiddetini hesaplamaktır. Simülasyon ve saha verilerinde ortalama %0.021 hata oranıyla önerilen yöntemle kırpışma hesaplanabileceği gösterilmiştir. Harmoniklerinin ve araharmoniklerinin gerçek zamanlı tespiti konusunda, elektrik ark ocağının (EAF) zamanla değişen harmoniklerini ve ara harmoniklerini doğru bir şekilde elde etmek için derecesi optimize edilmiş üstel yumuşatma (ES) ile birlikte kullanılan çoklu senkronize referans çerçevesi (MSRF) bazlı bir analiz yöntemi önerilmiştir. Gerçek zamanlı çalışma için, paralel işleme yapılmış ve grafik işleme birimi (GPU) ile çalışılmıştır. Saha verilerinde, uygulanan sinyalin 50. harmoniğe kadar olan tüm harmonikleri ve araharmonikleri 5 Hz çözünürlükte gerçek zamanlı olarak başarılı bir şekilde kestirilmiş ve simülasyon ortamında harmoniklerin ve araharmoniklerin aktif olarak filtrelenmesi başarıyla gerçekleştirilmiştir. Son olarak, GK olaylarının sınıflandırılması için, derin öğrenme yaklaşımına dayalı yeni bir yöntem sunulmuştur. Önerilen yaklaşımın yeniliği, güç şebekesinin üç fazındaki gerilim dalga biçimlerinin görüntü dosyalarının sınıflandırılmasıdır. Bir yıl boyunca elektrik iletim sisteminin dört trafo merkezinden elde edilen PQ olayları, önerilen sınıflandırma yönteminin eğitimi ve test edilmesi için kullanılmış ve potansiyel PQ olaylarına karşı otomatik bir karşı önlem geliştirilebileceği gösterilmiştir.

Bilim Kodu	: 90517
Anahtar Kelimeler	: Aktif Güç Süzgeci, Elektrik Ark Ocağı, Üstel Yumuşatma, Çok Katmanlı Evrimsel Sinir Ağları (ML-CNN), Grafik İşleme Birimi (GPU), Harmonik Çözümleme, Araharmonikler, Güç Kalitesi (GK-PQ), Çoklu Senkron Referans Çerçevesi (MSRF), Işık Kırpışması, GK Olayları, Sınıflandırma, Derin Öğrenme
Sayfa Adedi	: 60
Danışman	: Prof. Dr. Özgül SALORDURNA

DEVELOPMENT OF EFFICIENT ALGORITHMS FOR FLICKER, HARMONICS
AND INTERHARMONICS ESTIMATIONS AND POWER QUALITY EVENT
CLASSIFICATION SPECIALLY DESIGNED FOR HIGHLY TIME-VARYING
LOADS OF POWER SYSTEMS

(Ph. D. Thesis)

Ebrahim BALOUJI

GAZİ UNIVERSITY

GRADUATE SCHOOL OF NATURAL AND APPLIED SCIENCES

June 2019

ABSTRACT

The aim of this thesis is to develop tools which will provide complementary solutions to develop a complete and smart power quality (PQ) monitoring system. Based on the survey carried out on the current literature on PQ analysis and commercial devices, three main problems have been defined and solutions have been provided: the need of memory- and operation-efficient algorithms to estimate flicker, online detection of harmonics and interharmonics for highly time-varying load cases, and accurate PQ event classification. To estimate flicker from voltage RMS waveform, a digital realisation of the IEC (International Electrotechnical Committee) flickermeter using root mean square (RMS) of the voltage waveform as its input, instead of the voltage waveform, is presented. The aim is to compute the flicker severity according to the IEC flickermeter standard, IEC 61000-4-15, when only the RMS values of the voltage waveform are available. It has been shown on simulation and field data that short-term flicker severity can be computed by the proposed method with an average error rate of 0.021%. For the real-time detection of harmonics and interharmonics of current waveform, a multiple synchronous reference frame (MSRF) based analysis method is used together with order-optimized exponential smoothing (ES) to accurately obtain the time-varying harmonics and interharmonics of electric arc furnace (EAF) currents. Parallel processing of all harmonics and interharmonics are achieved by graphical processing unit (GPU). It has been shown on field data that the implemented system is capable of successfully estimating all harmonics up to the 50th and all interharmonics at 5 Hz resolution in real-time. Moreover, active filtering of certain harmonics and interharmonics has been successfully achieved in the simulation environment. Finally, a new method for the classification of PQ events based on deep learning (DL) approach is presented. Novelty of the proposed method is that, image files of the voltage waveforms of the three phases of the power grid are classified. PQ events obtained from four transformer substations of the electricity transmission system for a year are used for training and testing the proposed classification method. The proposed method is shown to be able to classify the PQ events collected in the field.

Science Code : 91440

Key Words : Active power filter, Electric arc furnace (EAF), Exponential smoothing (ES), Multi-layer convolution neural network (ML-CNN), Graphical Processing Unit (GPU), Harmonic Analysis, Interharmonics, Power Quality (PQ), Multiple Synchronous Reference Frame (MSRF), Light Flicker, PQ Event, Classification, Deep Learning (DL)

Page Number : 60

Supervisor : Prof. Dr. Özgül SALORDURNA

ACKNOWLEDGEMENTS

There are no proper words to convey my deep gratitude and respect for my thesis and research advisor, Professor Özgül SALOR-DURNA. She has inspired me to become an independent researcher and helped me realize the power of thinking and reasoning. I deeply thank my family for their unconditional trust, timely encouragement, and endless patience. It was their love that raised me up again when I got weary.



CONTENTS

	Page
SUMMARY	iv
ABSTRACT	v
THANKS	vi
CONTENTS	vii
LIST OF TABLE	ix
LIST OF FIGURES	xiv
SYMBOLS AND ABBREVIATIONS	xv
1. INTRODUCTION	1
2. METHODOLOGY	7
2.1. Method Developed for Flicker	7
2.1.1. Expressing the instantaneous flicker sensation in terms of voltage RMS values.....	7
2.1.2. Computation of the instantaneous flicker sensation valuesm	12
2.1.3. The proposed method for flicker severity computation	13
2.2. Methods Developed for Harmonics and Interharmonics Estimation in Real-Time	14
2.2.1. MSRF + exponential smoothing method for the fundamental, harmonic and interharmonic analysis	15
2.2.2. Exponential smoothing technique for low pass filtering	19
2.3. Method Developed for Power Quality Event Classification	25
2.3.1. Architecture overview	29
3. RESULTS AND DISCUSSION	35
3.1. Results for Flickermeter	35
3.1.1. Verification of the proposed method using synthetic voltage waveforms.....	35
3.1.2. Verification of the proposed method using field data.....	38

	Page
3.2. Results and Discussion on Real Time Detection of Harmonic and Interharmonics	41
3.3. Results for Classification of PQ Events	45
4. CONCLUSION	49
REFERENCES	53
CURRICULUM VITAE	59



LIST OF TABLES

Table	Page
Table 2.1. Normalised flickermeter response for sinusoidal voltage fluctuations, 230 V/50Hz systems, which result in unity instantaneous flicker sensation, S – IEC standard 61000-4-15 [2].....	14
Table 2.2. PQ event data obtained from the transmission system (1337 events in total)	28
Table 2.3. PQ event data lables obtained manually for all the events listed in.....	28
Table 3.1. Mean of flicker sensation (S) values obtained by the proposed method using signal RMS values and by the IEC flickermeter using voltage waveform	37
Table 3.2. Mean of instantaneous flicker sensation, S, values and the flicker severity, Pst, obtained by the standard IEC flickermeter and the proposed method (PM) from field data (10-min voltages obtained at a transformer Substation supplying an EAF plant)	40
Table 3.3. Comparison of the flicker severities obtained by the IEC flickermeter and The proposed method (PM)	40
Table 3.4. Processing times of one-min EAF current data for MSRF+ES, and MSRF+KF on CPU, and MSRF+Es implemented on NVIDIA geforce GTX 960 graphics card (GPU).....	43

LIST OF FIGURES

Figure	Page
Figure 2.1. A sample sine wave component at any flicker frequency, f_{fi} , with the integration intervals, $T/2$, equal to half the period of the fundamental frequency. Integration will approximately yield the value of the signal sample at the mid point of the integration period scaled by $T/2$	11
Figure 2.2. Amplitudes of the flicker frequency components (ΔV_i) versus the corresponding flicker frequencies, f_{fi} , using the proposed flicker frequency decomposition method for the voltage waveform generated using	12
Figure 2.3. Obtaining the field data used in this research work; (a) schematic of the data collection at the measurement point (MP) and the proposed systems, (b) sample three-phase current waveform obtained from the boring phase of the EAF current, (c) 10-cycle RMS of the EAF current for Phase-A for a period of 60 min (BP: boring period, MeP: Melting Period, RP: Refining Period).	17
Figure 2.4. Extraction of the fundamental (50 Hz) component and the rest of all harmonic and interharmonic components	18
Figure 2.5. Frequency component estimation block: MSRF+ES application to obtain any frequency component	18
Figure 2.6. Comparison of the original EAF current spectrum (blue) with the extracted fundamental component spectrum using MSRF+ES (red) for exponential smoothing with an order of size (a) 10ms, (b) 300 ms, (c) 140 ms, which is the best in terms of undamental estimation and low THID, and (d) using MSRF with KAlman filtering	21
Figure 2.7. THID and amplitude error (AE) computation for any frequency component to obtain the best order of ES for each	22
Figure 2.8. Comparison of the original EAF current spectrum (blue) with the extracted second harmonic component spectrum using MSRF+ES (red) for exponential smoothing with a order of (a) 160 ms, (b) 10 ms, (c) 80 ms, which is the best in terms of fundamental estimation and low THID, (d) using MSRF with Kalman filtering	23
Figure 2.9. Amplitude error of the MSRF+ES estimation compared to the original waveform component with respect to ES order for the fundamental frequency (50Hz), and interharmonics at 45 Hz and 55 Hz Error is computed for a typical boring phase period of 10-min cycles (mean error of 3000 10 cycles of the fundamental) as the percent of the original frequency component amplitude	24

Figures	Page
Figure 2.10. THID for the fundamental (50 Hz) and interharmonics at 45 HZ and 55 HZ obtained from the MSRF+ES for a typical boring phase period of 10 min cycles (mean error of 3000 10 cycles of the fundamental).....	25
Figure 2.11. The PQ monitoring system architecture.....	27
Figure 2.12. Sample sag event in two-phases and swell in the other phase, (a) RMS voltages of each phase, (b) arranged event data in a single row vector	27
Figure 2.13. Image net classification with deep convolutional neural networks	30
Figure 2.14. Layer structure of a (a) NN, (b) MLCNN	31
Figure 2.15. Examples: (a) first two steps of the convolving procedure for a 7x7 data matrix by a 3x3 weighting matrix, (b) application of MAXPool function with a 2x2 filter with two units of shifting.....	32
Figure 2.16. Flow chart of the implemented deep learning algorithm in this work, obtained by DIGITS deep learning application platform.....	33
Figure 3.1. Digital realization of the proposed flickermeter using RMS of the voltage waveforms, a) The general block diagram, b) Details of the signal processing in Block-A and Block-B.....	36
Figure 3.2. Half-cycle RMS of the three-phase voltage waveforms obtained from a transformer substation supplying an EAF plant, a Phase-A, b) Phase-B, c) Phase-C.	39
Figure 3.3. Instantaneous flicker sensation values, S, obtained by the digital realization of the IEC flickermeter (blue) and the proposed method (green) corresponding to a voltage data of 10 minutes obtained from a transformer substation supplying an EAF plant.....	40
Figure 3.4. Block diagram of the GPU-accelarated MSRF+ES method implemented on NVIDIA Geforce GTX 960 graphics card	41
Figure 3.5. The optimum orders ($T_{opt}(f)$) of MSRF+ES analysis obtained as the solution of the optimization problem defined in (2.20) for the most typical EAF boring phase harmonics and interharmonics	42
Figure 3.6. Positive sequence d component for the fontamental frequency together with its DC component obtained by KAlman Filter and ES.....	43

Figures	Page
Figure 3.7. Comparison of the original EAF current with the reconstructed EAF current waveform, constructed by summing up the estimated frequency components with MSRF+ES method (fundamental, harmonics at 2 nd and odd ones up to 30 th, and interharmonics with 5 Hz resolution up to 150 Hz).....	44
Figure 3.8. Comparison of the DFT spectrums of the original current Phase-A current waveform of 10 cycles (blue) and (a) that of waveform from which the components at 95 HZ, 100 HZ, and 105 HZ obtained by MSRF+Es with optimal ES orders are substracted (red); (b) that of waveform from which the components at 30 HZ, 55 HZ, 60 HZ, and 65 HZ obtained by MSRF+ES with optimal ES orders are substracted (red), to simulate an APF operation.....	45
Figure 3.9. Loss and accuracy versus epoch number during the MLCNNN training ..	46
Figure 3.10. Examples of interruption event images out of the PQ event data used for test with the predicted event types using deep learning in DIGITS platform, (a) interruption in three phases, (b) interruption in two phases..	46
Figure 3.11. Examples of dip and swell event images out of the RQ event data used for test with the predicted event types using deep learning in DIGITS platform, (a) long dip in one phase, (b) dip in three phases.....	47

SYMBOLS AND ABBREVIATIONS

The symbols and abbreviations used in this study are presented below, along with their descriptions.

Symbols	Descriptions
----------------	---------------------

s	Second
----------	--------

Hz	Hertz
-----------	-------

Abbreviations	Descriptions
----------------------	---------------------

PQ	Power quality
-----------	---------------

MLCNN	Multi-layer convolution neural network
--------------	--

APF	Active power filter
------------	---------------------

ES	Exponential smoothing
-----------	-----------------------

EAF	Electric arc furnace
------------	----------------------

GPU	Graphical processing unit
------------	---------------------------

RMS	Root mean square
------------	------------------

1. INTRODUCTION

In this thesis, development of efficient and fast algorithms for flicker, harmonics, interharmonics and power quality events developed specifically for harsh conditions, such as the existence of intermittent loads, in the power systems is the main focus. The effort towards this focus in this research work can be presented under three main topics: (i) computation of light flicker, (ii) extraction of power system harmonics and interharmonics, and (iii) power quality event classification. All the analyses have been developed and tested on both synthetically generated voltage and current waveforms and field data collected from the transmission substations of the electricity transmission system of Turkey, located around the intermittent loads such as electric arc furnace plants. In this section, a detailed literature review is presented on all of the above listed three topics.

Light flicker refers to quick and repeated changes in the light intensity caused by the amplitude fluctuations of the voltage supplying the lamp and it can be measured directly from the voltage waveform, as recommended by the IEC standard, IEC 61000-4-15 [2]. Light flicker is caused due to the low-frequency fluctuations of the voltage magnitude and a 10-min raw data of the voltage signal is required to obtain the short-term flicker severity [2], which is not always easy to achieve due to memory limitations. There are various approaches in the literature for the computation of light flicker [3 - 14], yet there is no study which directly computes the light flicker in the absence of the voltage waveform, but presence of its RMS form instead, except for the work reported in [8]. In [8]; however, four of the five blocks of the IEC flickermeter are used, but RMS computation is used to obtain the signal envelope instead of the first block of the IEC flickermeter [2]. The root-mean-square (RMS) method is widely used in quantifying the effective magnitude of an alternating current (AC) signal. In power-quality (PQ) analysis, the RMS value of the voltage is used for the characterization of PQ events, such as voltage sags and swells, as well as for quantifying voltage or current variations [1]. Based on the PQ measurement standard IEC-61000-4-30 [1], RMS value of a signal is usually calculated from a half-cycle- or a one-cycle-length window. In many PQ analysis systems and devices, RMS values of the voltage and current waveforms are stored instead of the raw data, for later analyses and evaluations, due to the fact that storage of the raw data is not practical and is extremely expensive.

The main concern of the research work presented in the first part of this thesis is developing a method, which can measure the light flicker from the RMS values of the voltage, instead of the voltage waveform itself. Such a case can occur, for example, when flicker analysis is required on previously recorded RMS voltage waveforms, but there exist no sampled voltage data. The proposed method in this thesis provides a solution to this problem by analyzing the RMS values of a voltage waveform in terms of its flicker frequency components.

The second main topic of this thesis, which is the detection of the harmonics and interharmonics of the power system has been a hot and challenging topic of research, especially when the current and voltage waveforms are non-stationary with time-varying components as in the case of an Electric Arc Furnace (EAF) [21-45]. [21] provides classification and comparison of various time-varying harmonics and interharmonics detection methods existing in the literature by 2014. In [21], among short-time Fourier Transform (STFT), ESPRIT- and Prony-based methods, ADALINE-based methods, Kalman filtering, PLL-based methods, and artificial neural network (ANN)-based methods, only ANN- and Kalman-based methods are claimed to be suitable for real-time applications, under certain conditions such as similar type of loads, and etc. In [29], Prony's method is used to extract exact frequency of voltage variations because measuring accurate frequencies is undeniable when the extracting of voltage characterization comes into account. The use of PLLs for harmonics and interharmonics detection has been studied in [36- 39], while Kalman-based methods have been proposed in [40]. In the recent years multiple synchronous reference frame (MSRF)-based methods have been popular [24] and [41-56], due to the fact that MSRF provides time-domain waveform for each harmonic and interharmonic frequency; however, the need for low-pass filtering in the MSRF analysis is the bottle-neck of the method in terms of processing-time. In order to minimize the time for the low-pass filtering (LPF) in the MSRF analysis, Kalman filtering has been proposed and applied in [24], and it has been shown that LPF delay is reduced significantly; however, Kalman filtering (KF) provides estimations with variable delays depending on the data statistics. The use of graphical processing units (GPU) has been considered in [45] to make the MSRF analysis with KF method real-time. With the use of GPU, parallel processing of all harmonics and interharmonics have been shown to be possible [45]. GPUs have been widely used in different areas, especially in image processing applications, but they have also been popular recently in the power electronics and power systems area [45-48].

Electric Arc Furnaces (EAF) are one of the most interesting harmonic and interharmonic generators of the electric grids with highly stochastic nature of operation and the resulting currents with time-varying harmonics and interharmonics. EAF currents are rich in interharmonics between the fundamental and the second harmonic resulting in seriously distorted point of common coupling (PCC) voltages also with flicker, from which EAF plants are supplied [17-19]. In order to improve the quality of power at the PCC, time-varying EAF current harmonics and interharmonics have to be analyzed fast and accurately so that reference signals are supplied to the controllers of the advanced technology compensation systems such as active power filters (APF), synchronous static compensators (STATCOM) and energy storage systems (ESS) [20].

The second aim of the research work presented in this thesis is to detect of harmonics and interharmonics in real-time. An MSRF-based method is proposed together with Exponential Smoothing (ES) as the LPF on a GPU framework for the real-time analysis of time-varying harmonics and interharmonics of current waveforms obtained from an EAF plant supplied from the electricity transmission system. ES has been especially proposed for prediction of direct current (DC) level component of market trends in economics [49-53]. Recently, it has also been used for information technology applications and load forecasting in power grids [49]. In this thesis, ES has been used in the MSRF analysis for the low-pass filtering, which is the bottle neck of the processing time for harmonics and interharmonics analysis. ES is used to low-pass filter the positive- and negative-sequences of both d and q components of three-phase harmonic and interharmonic voltage and current components. Order of ES application has been optimized for each frequency component so that amplitude estimation for each frequency component is maximized while minimizing the erroneous and unexpected component amplitudes in the computation. ES with optimized order has been shown to provide accurate harmonic and interharmonic estimates with less delay than the use of KF with MSRF, hence resulting in more accurate amplitude and phase estimates of the frequency components. Implementation of the proposed MSRF+ES algorithm for each frequency component in parallel on an NVIDIA Geforce GTX 960 graphics card has led real-time analysis of actual EAF currents obtained from the field. The preference of the use of GPUs for parallel processing analysis instead of FPGAs is that, not only the GPUs are cheaper but also thanks to a lot of memory access, they are capable of handling high-level languages such as CUDA and C++. On the other hand, less

level of complexity is needed for GPU programming compared to FPGAs. Finally, It is easy to update a task on GPU based system since in FPGA based system the hardware update will be required which is costly [53].

The third and the final aim of this thesis is to classify PQ events, such as voltage sags, swells or interruptions. While PQ is defined as the wellbeing of electrical power for consumer devices by the IEC Standard 61000-4-30 [1], PQ event is defined as the deviation of PQ out of a predefined tolerance band. The reason that makes PQ events to be taken into consideration seriously is that they can be the possible reasons of malfunctioning of the electrical equipment in the system or they can even lead to brownouts or blackouts in the electricity system. By means of a long-term monitoring of PQ in any electricity grid, at one of its generation, transmission or distribution level, huge amount of PQ event data will be available for studying the system characteristics or taking countermeasures to improve the quality of power. Therefore, PQ event data, collected according to the harmonic standard IEC 61000-4-7 [54], should be clustered and classified to comprehend and improve the PQ in an electricity grid.

For the purpose of analyzing PQ event data, significant amount of effort is reported in the literature [55-66]. In [57], classification of harmonics by using k-means clustering and Support Vector Machine (SVM) algorithm is proposed. Automatic PQ event data clustering based on eigenanalysis followed by k-means clustering is achieved in [58]. Using k-means together with Principle Component Analysis (PCA), Linear Discriminant Analysis (LDA) and Singular Value Decomposition (SVD) for the clustering of PQ events are compared in [59]. An expert system, which is able to classify voltage dips and interruptions, is proposed in [62]. An automatic classification, whose policy is to apply empirical-mode decomposition and Hilbert transform on PQ Events, is reported in [63]. [64] has done PQ assessment with the application of two empirical mode decomposition based de-noising techniques in cases of noisy event data. [66] uses Stockwell's transform and NN-based classifier to detect multiple PQ disturbances following each other.

In the final part of the research work presented in this thesis, deep learning, which is a powerful classifier in cases of huge data for train, is employed for PQ event data analysis. In contrast with the existing PQ event data analysis techniques, sampled voltage data of the PQ events are not used, but image files of the PQ events are analyzed by taking the

advantage of the success of the deep learning approach on image-file-classification. Therefore, the novelty of the proposed approach is that, images of the voltage waveforms of three phases of the power grid are classified with almost 100% accuracy, instead of classifying the sampled voltage data strings of the three phases [65].

There exists a large amount of deep learning publications in other research areas, e.g. computer vision/image processing area, which can be applicable for PQ event classification. Deep learning methods, in some areas, have already exceeded human performance, e.g., playing the game of Alpha Go without human intervention [69]. CNNs, recurrent neural networks (RNNs), and recurrent convolutional networks (RCNs) have been successfully employed in automatic image/video feature learning, e.g., in face recognition from images [70], handwritten digit recognition from images [68], human fall detection and human activity classification [71] from videos. These deep learning methods enable automatic feature learning for the dedicated signals when big data is available. The successful research in these areas inspired us to develop dedicated deep learning methods for automatic feature learning of PQ events and subsequently use them for PQ event classification.

In summary, this thesis consists of three parts presenting novel and efficient methods for light flicker evaluation, online power system harmonics and interharmonics detection and PQ event classification. All the methods developed have been shown to overperform compared to the methods in the literature in terms of computational complexity and being suitable for real-time applications. In Chapter 2 of the thesis, methodologies developed for all three aims are explained in subsections. In Chapter 3, results are provided and discussed for all three methods on both synthetically generated and field data obtained from the electricity transmission system of Turkey. Finally Chapter 4 provides the conclusions.



2. METHODOLOGY

In this chapter, the methods used to develop the proposed algorithms are discussed under three subsections. The first subsection will present the developed method to estimate the flicker according to IEC flickermeter method from true RMS values of the voltage waveform. Then the second subsection addresses the methodologies developed for real time detection of harmonics and interharmonics out of EAF current waveforms to generate reference signals for possible active power filter applications of highly time-varying power signals. In the third subsection, the developed deep learning based method for classification of PQ events are presented.

2.1. Method Developed for Flickermeter

In this subsection, the methodology developed to estimate the flicker from rms values is described.

2.1.1. Expressing the instantaneous flicker sensation in terms of voltage RMS values

As the IEC standard proposes [2], the flicker-causing fluctuation of the voltage can be modelled as an amplitude modulated (AM) signal, where the power system frequency (50 or 60 Hz) is the carrier frequency and the flicker frequency is the message frequency as given in (2.1),

$$v(t) = V \sin(2\pi ft) \left\{ 1 + \frac{1}{2} \frac{\Delta V}{V} \sin(2\pi f_f t + \emptyset) \right\}, \quad (2.1)$$

where f_f is the frequency of the flicker, f is the fundamental frequency of the power system, which can be 50 or 60Hz, V is the amplitude of the fundamental component, ΔV is the amplitude of the flicker component, and \emptyset is its phase. In cases when the voltage signal carries several flicker components, in other words, if the voltage envelope varies in a more complicated manner including more than one frequency component, $v(t)$ can be expressed in a more general form as given in (2.2),

$$v(t) = V \sin(2\pi ft) \left\{ 1 + \sum_{i=1}^N \frac{1}{2} \frac{\Delta V_i}{V} \sin(2\pi f_{f_i} t + \phi_i) \right\}. \quad (2.2)$$

In (2.2), N is the number of flicker frequency components forming the envelope of the signal, f_{f_i} are the flicker frequencies, and ϕ_i are the corresponding phases.

Now the RMS value of the voltage waveform in (2.2) can be evaluated. The most popular formula for RMS computation of a continuous voltage waveform, $v(t)$, is given in (2.3),

$$V_{RMS} = \left(\frac{1}{T} \int_0^T v(t)^2 dt \right)^{1/2}, \quad (2.3)$$

where T is the period of the fundamental component of the voltage waveform. Now if half-cycle RMS of $v(t)$ in (2.2) is computed as recommended in [1], the expression in (2.4),

$$V_{RMS} = \sqrt{\frac{2}{T} \int_0^{T/2} \left\{ \underbrace{V \sin(2\pi ft) + \frac{1}{2} \sin(2\pi ft) \sum_{i=1}^N \Delta V_i \sin(2\pi f_{f_i} t + \phi_i)}_A \right\}^2 dt}, \quad (2.4)$$

is obtained. T in (2.5) is ideally 20 ms for the power system frequency at exactly 50Hz. Evaluating the square inside the integral, denoted by A in (4), yields the expression in (2.5),

A

$$= \left\{ \begin{aligned} & V^2 \sin^2(2\pi ft) + \frac{1}{4} \sin^2(2\pi ft) \sum_{i=1}^N \Delta V_i \sin(2\pi f_{f_i} t + \phi_i) \sum_{j=1}^N \Delta V_j \sin(2\pi f_{f_j} t + \phi_j) \\ & + V \sin^2(2\pi ft) \sum_{i=1}^N \Delta V_i \sin(2\pi f_{f_i} t + \phi_i) \end{aligned} \right\} \quad (2.5)$$

Taking the square of the both sides of the equation in (2.4) and then taking the first term inside the integral to the left side of the equation, (2.6) is obtained as

$$\begin{aligned}
V_{RMS}^2 &= \underbrace{\frac{2}{T} \int_0^{\frac{T}{2}} V^2 \sin^2(2\pi ft) dt}_B \\
&= \frac{1}{2T} \int_0^{\frac{T}{2}} \sin^2(2\pi ft) \underbrace{\sum_{i=1}^N \Delta V_i \sin(2\pi f_{f_i} t + \phi_i) \sum_{j=1}^N \Delta V_j \sin(2\pi f_{f_j} t + \phi_j)}_C dt \\
&\quad + \underbrace{\frac{2}{T} \int_0^{\frac{T}{2}} V \sin^2(2\pi ft) \sum_{j=1}^N \Delta V_j \sin(2\pi f_{f_j} t + \phi_j) dt}_D . \tag{2.6}
\end{aligned}$$

In (2.6), square of V_{RMS} is the square of the true RMS of the voltage waveform and it can be obtained from the voltage waveform directly by computing the half-cycle RMS. The second term, B , on the left side of (2.6) can be computed by calculating the square of the mean of all V_{RMS} values over the voltage data for which flicker is to be evaluated. That is because B is expected to be constant over all data for all half-cycle windows, being the square of the RMS value of only the fundamental component evaluated at exactly its half period. Therefore, it can be considered as the mean value of the square of the RMS of the voltage signal with no fluctuations. Hence, left-hand-side of (2.6) can be expressed as a function of V_{RMS} , and can be called as $F(V_{RMS})$.

In (2.6), C can be considered to be negligibly small with respect to D since the amplitude of C is scaled by the multiplication of ΔV_i and ΔV_j , while D is scaled by the multiplication of V and ΔV_i . Being the amplitude of the flicker components of the voltage waveform, ΔV_i is expected to be much smaller than the amplitude of the fundamental, V . Hence, (2.6) can be approximately expressed as given in (2.7)

$$F(V_{RMS}) \cong \frac{2}{T} \int_0^{\frac{T}{2}} V \sin^2(2\pi ft) \sum_{i=1}^N \Delta V_i \sin(2\pi f_{f_i} t + \phi_i) dt. \tag{2.7}$$

Evaluating the right-hand side of (2.7), by using the expansion of the sine square, the expression in (2.8),

$$F(V_{RMS}) \cong \frac{1}{T} \left\{ \int_0^{\frac{T}{2}} \sum_{i=1}^N V \Delta V_i \sin(2\pi f_{f_i} t + \phi_i) dt - \underbrace{\int_0^{\frac{T}{2}} \sum_{i=1}^N V \Delta V_i \cos(4\pi f t) \sin(2\pi f_{f_i} t + \phi_i) dt}_E \right\}, \quad (2.8)$$

is obtained. E in (2.8) yields two sine components with frequencies $2f+f_{f_i}$ and $2f-f_{f_i}$ and integration of those sine components at an interval, which corresponds to the half-cycle of the fundamental frequency, results in values close to zero, since flicker frequencies f_{f_i} are much smaller than $2f$. Since the expansion of E in (2.8) is rewritten as in (2.9),

$$E = \frac{1}{2} \left(\int_0^{T/2} \sum_{i=1}^N V \Delta V_i \sin(4\pi f t + 2\pi f_{f_i} t + \phi_i) dt - \int_0^{T/2} \sum_{i=1}^N V \Delta V_i \sin(4\pi f t - 2\pi f_{f_i} t - \phi_i) dt \right). \quad (2.9)$$

Hence, (8) can be approximated as given in (10),

$$F(V_{RMS}) \cong \frac{1}{T} \int_0^{\frac{T}{2}} \sum_{i=1}^N V \Delta V_i \sin(2\pi f_{f_i} t + \phi_i) dt. \quad (2.10)$$

The expression in (2.10) is the basis of the flicker computation method proposed in this research work. $F(V_{RMS})$ is expressed as in (2.11),

$$F(V_{RMS}) = V_{RMS}^2 - \frac{2}{T} \int_0^{\frac{T}{2}} V^2 \sin^2(2\pi f t) dt, \quad (2.11)$$

and it can be computed directly from the voltage waveform, if it exists, or it can be computed from the half-cycle RMS values of the voltage signal. As to the right-hand side of (2.10), since the integration period, $T/2$, is much smaller than the period of the flicker frequency components, f_{f_i} , integration will yield the same frequency components, f_{f_i} , with

an approximate scaling factor of $T/2$, which is illustrated in Figure 2.1. In Figure 2.1, the sine wave represents one of the flicker frequency components and the integration periods are illustrated by $T/2$, which corresponds to the half the fundamental period. The integration over very small intervals with respect to the period of the signal will result in values, which will oscillate with the same frequency of the flicker frequency component. Integration will approximately yield the value of the signal sample at the mid point of the integration period scaled by $T/2$. Hence, obtaining the Discrete Fourier Transform (DFT) of F (V_{RMS}), computed from the voltage waveform or its RMS values, flicker frequency components, f_{fi} , and the corresponding amplitudes, ΔV_i , can be obtained.

To illustrate the proposed flicker frequency determination method, a synthetic signal with three flicker frequency components at 3.5Hz, 10Hz and 15Hz has been generated, as given in (2.12),

$$v(t) = \sin(2\pi ft) \left\{ 1 + \left(\frac{1}{2}\right) 0.045\sin(2\pi 3.5t) + \left(\frac{1}{2}\right) 0.020\sin(2\pi 10t) + \left(\frac{1}{2}\right) 0.010\sin(2\pi 15t) \right\}, \quad (2.12)$$

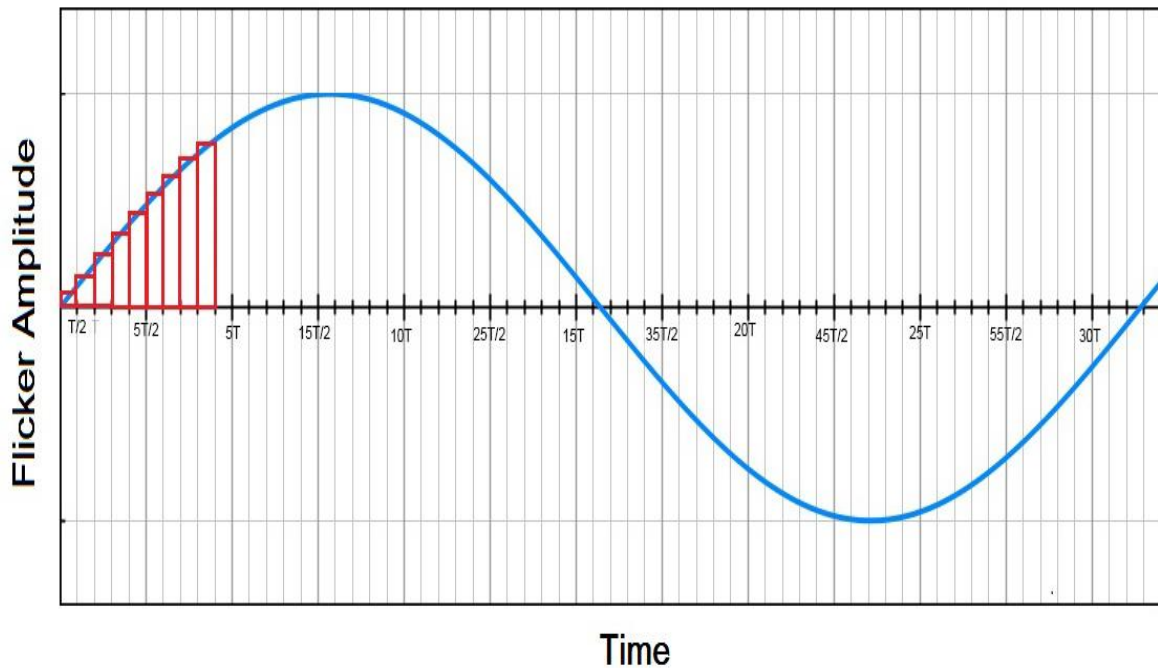


Figure 2.1. A sample sine wave component at any flicker frequency, f_{fi} , with the integration intervals, $T/2$, equal to half the period of the fundamental frequency. Integration will approximately yield the value of the signal sample at the mid point of the integration period scaled by $T/2$

where, f denotes the fundamental frequency, which is 50Hz. The amplitudes of the flicker frequency components have been selected to be 1%, 2%, and 4.5% of the fundamental component, respectively, which are common ratios for a real-life voltage signal [7]. $F(V_{RMS})$ in (2.11) has been computed for the generated waveform $v(t)$ in (2.12) and the amplitude of its DFT is shown in Figure 2.2, which shows that the flicker frequency components can be determined by detecting the components with amplitudes higher than a threshold. The other components with negligibly small amplitudes around 5Hz, 6Hz, 11Hz, and 13Hz correspond to the components neglected in (2.6). The neglected term C in (2.6), includes frequency components at the summations and differences of individual frequency components. Therefore, the synthetic signal in (2.12), is expected to have frequency components at 13.5Hz, 6.5Hz, 11.5Hz, 18.5Hz, 5Hz, and 25Hz with negligibly small amplitudes, which is observed in Figure 2.2.

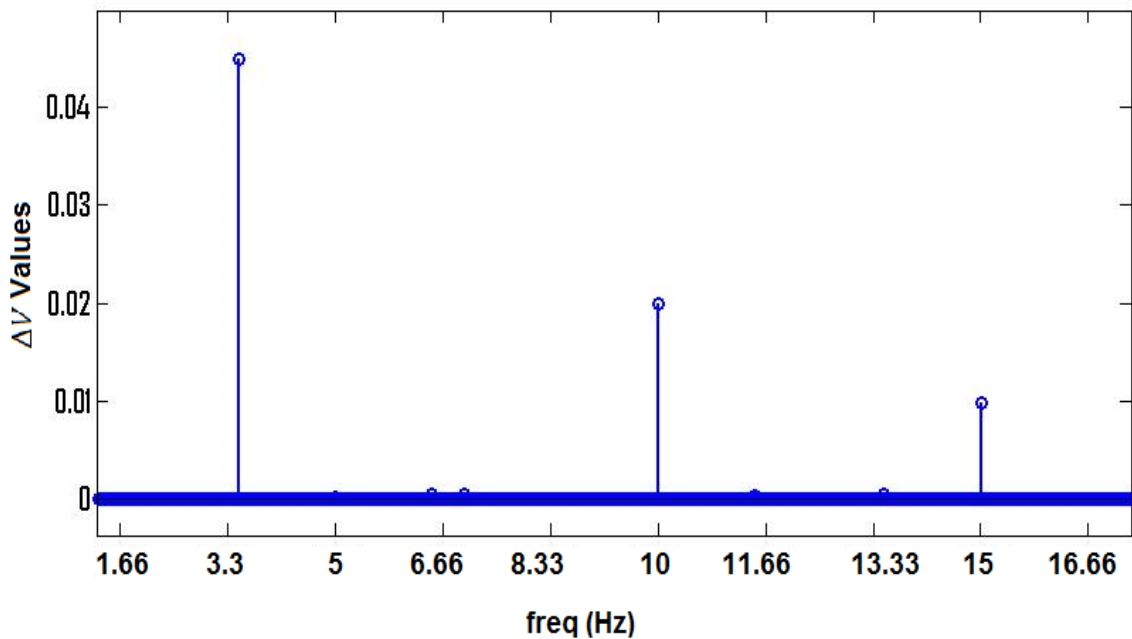


Figure 2.2. Amplitudes of the flicker frequency components (ΔV_i) versus the corresponding flicker frequencies, f_{fi} , using the proposed flicker frequency decomposition method for the voltage waveform generated using (12)

2.1.2. Computation of the instantaneous flicker sensation values

The IEC flickermeter response for sinusoidal fluctuations with flicker frequencies and $\Delta V/V$ amplitude ratios for the signal model given in (2.1), which result in unity instantaneous flicker sensation ($S = 1$) are listed for 230 V/ 50 Hz systems in Table 2.1 [2].

Instantaneous flicker sensation, S , is a measure of the sensation of human beings of the voltage fluctuation effect on an incandescent lamp and it is the output of the Block-4 of the IEC flickermeter, which is given in [2]. When $S = 1$, it means that at least 50% of the human beings realize the fluctuation of the voltage [2].

It has been shown in a previous work in [7] that S is approximately equal to the summation of the flicker-causing effects of the individual flicker frequency components, f_{fi} in (2.2), as given in (2.13). Contribution of each flicker frequency to S , which is represented here by S_i , can be attained by comparing the square of the $\Delta V/V$ values obtained from the voltage waveform to the $\Delta V/V$ values obtained from Table 2.1, denoted by $(\Delta V/V)_{IEC}$, for each flicker frequency. ΔV_i is obtained from the Fourier Transform amplitudes of the signal in (2.10) and V can be obtained from mean of calculated RMS value of the signal.

$$S_i = \frac{\left(\frac{\Delta V_i}{V}\right)^2}{\left(\frac{\Delta V_i}{V}\right)_{IEC}^2} \quad (2.13)$$

The instantaneous flicker sensation, S , is obtained as the summation of all S_i , $S = \sum S_i$, for which f_{fi} varies from 0.5 to 25.0 Hz with 0.5 Hz increments when the FFT window size is 100 cycles of the fundamental period (2-s), and hence the frequency resolution of the DFT is 0.5Hz. This method inherently includes both the effect of the human eye sensitivity and the effect of the incandescent lamp sensitivity to voltage fluctuations, which is realized in the third block of the IEC flickermeter, because the denominator of (2.13) contains the voltage fluctuation level which causes average flicker sensitivity equal to unity at the output of Block-4 of the IEC flickermeter [7].

2.1.3. The proposed method for flicker severity computation

The block diagram of the proposed flicker severity computation method using RMS values of the voltage waveform is illustrated in Figure 2.3 (a). Block-A in Figure 2.3 (a) illustrates the computation of the decomposition of the flicker frequency components using the RMS values of the voltage waveform, explained in detail in Section 2. Block-B represents the computation of the instantaneous flicker sensation values, S , from the decomposed flicker frequency components. The third and the final block is the statistical analysis block, which

is the same as Block-5 of the IEC flickermeter given in 2]. The third block in Figure 2.3 (a) analyses the instantaneous flicker sensation values, S , for a 10-min period to provide the short-term flicker severity, P_{st} . Details of the instantaneous flicker sensation computation inside Block-A and Block-B in Figure 2.3 (a) is illustrated in Figure 2.3 (b). Each frame in Figure 2.3 (b), includes squares of the half-cycle RMS values, from which mean square of the RMS values inside that frame are subtracted. Frames include 200 values, which means 2-s data (i.e. 200 half-cycle values make 100 values per second for a 50Hz system). Hence the DFT resolution for 2-s frames corresponds to a frequency resolution of 0.5Hz. Then from each DFT frame, flicker frequencies, f_{fi} , and the corresponding amplitudes, ΔV_i , are obtained using the method described in subsection 2.1.2 and an instantaneous flicker sensation value, S , is then obtained for each frame as detailed in subsection 2.1.3. Frames are shifted by two half-cycle-RMS samples, which correspond to S being obtained every cycle of the fundamental frequency. This is consistent with the requirement of the flickermeter standard that input for Block-5, which is the instantaneous flicker sensation S , should be sampled by at least 50Hz [2]. Once S is obtained, Block-5 of the IEC flickermeter is used to obtain short-term flicker severity, P_{st} , from 50x600 S samples, which correspond to the short-term flicker severity computation period of 10 minutes.

Table 2.1. Normalised flickermeter response for sinusoidal voltage fluctuations, 230 V/50Hz systems, which result in unity instantaneous flicker sensation, S – IEC standard 61000-4-15 [2]

Hz	$\frac{\Delta V}{V}$, %	Hz	$\frac{\Delta V}{V}$, %	Hz	$\frac{\Delta V}{V}$, %	Hz	$\frac{\Delta V}{V}$, %
0.5	2.340	5.0	0.398	10.0	0.260	17.0	0.530
1.0	1.432	5.5	0.360	10.5	0.270	18.0	0.584
1.5	1.080	6.0	0.328	11.0	0.282	19.0	0.640
2.0	0.882	6.5	0.300	11.5	0.296	20.0	0.700
2.5	0.754	7.0	0.280	12.0	0.312	21.0	0.760
3.0	0.654	7.5	0.266	13.0	0.348	22.0	0.824
3.5	0.568	8.0	0.256	14.0	0.388	23.0	0.890
4.0	0.500	8.8	0.250	15.0	0.432	24.0	0.962
4.5	0.446	9.5	0.254	16.0	0.480	25.0	1.042

2.2. Methods Developed for Harmonics and Interharmonics Estimation in Real-Time

In this subsection methods developed to extract real harmonics and interharmonics in real-time are explained. Application of the Multiple Synchronous Reference Frame (MSRF)

analysis with Exponential Smoothing (ES) and obtaining the best order of exponential smoothing specific to each harmonic and interharmonic component are presented in this section.

2.2.1. MSRF+exponential smoothing method for the fundamental, harmonic and interharmonic analysis

MSRF analysis is used to obtain both positive- and negative-sequences of d , q , and $zero$ components of all harmonics and interharmonics. Note that, since the EAF transformer is a Δ/Δ connected transformer, EAF currents obtained from the MP in Figure 2.3 (a) are balanced but asymmetrical due to the nature of the EAF operation [25]. Hence, the zero sequence components are zero for 99.9% of the operation time, therefore in this analysis zero sequences are equated to zero to compensate any measurement errors. After obtaining the direct current (DC) components of the positive- and negative sequences of the d and q components, they are transformed back to the phase current components so that one of the fundamental, harmonics, and the interharmonics is obtained. The DC components of the positive and negative-sequences of d and q components carry on both the amplitude and phase information of all three phases of the EAF current, corresponding to the selected frequency component. Starting with the three-phase EAF currents with the fundamental, and all possible harmonic and interharmonic components, three-phase current waveforms are as given in (2.14),

$$\begin{aligned}
 i_A(t) &= \sum_{i=0}^N A_i \sin(2\pi f_i t + \Phi_{A_i}) \\
 i_B(t) &= \sum_{i=0}^N B_i \sin(2\pi f_i t + \Phi_{B_i}) \\
 i_C(t) &= \sum_{i=0}^N C_i \sin(2\pi f_i t + \Phi_{C_i})
 \end{aligned} \tag{2.14}$$

where, f_i represents all the frequency components existing in the waveform, A_i , B_i , and C_i ; and Φ_{A_i} , Φ_{B_i} , and Φ_{C_i} are the corresponding amplitudes and phases, respectively. In order to give the idea of MSRF analysis and the low-pass filtering to obtain any of the frequency

components from the original current waveform here, only computation of the positive sequence d component is shown in (2.15):

$$\begin{aligned}
i_D^+(t) = & \sqrt{\frac{2}{3}} \sum_{i=0}^N \frac{A_i}{2} \sin(2\pi f_i t + \Phi_A) \cos(2\pi f t) \\
& + \sqrt{\frac{2}{3}} \sum_{i=0}^N \frac{B_i}{2} \sin(2\pi f_B t + \Phi_B) \cos\left(2\pi f t - \frac{2\pi}{3}\right) \\
& + \sqrt{\frac{2}{3}} \sum_{i=0}^N \frac{C_i}{2} \sin(2\pi f_C t + \Phi_C) \cos\left(2\pi f t + \frac{2\pi}{3}\right)
\end{aligned} \tag{2.15}$$

f in (2.15) is the frequency component for which the analysis is carried out, i.e. f is the frequency component which is looked for in the current waveform. If there is any f frequency component in the current waveform, then the DC component of (2.15) is going to be nonzero and hence the low-pass filtered form of the positive sequence d components is obtained as given in (2.16):

$$\begin{aligned}
i_D^{LP+}(t) = & \sqrt{\frac{2}{3}} \frac{A_k}{2} \sin(2\pi(f_k - f)t + \Phi_{A_k}) + \sqrt{\frac{2}{3}} \frac{B_k}{2} \sin(2\pi(f_k - f)t + \Phi_{B_k}) \\
& + \sqrt{\frac{2}{3}} \frac{C_k}{2} \sin(2\pi(f_k - f)t + \Phi_{C_k})
\end{aligned} \tag{2.16}$$

In (2.16), f_k is the frequency component, which is equal to or very close to the frequency f . If such an f_k exists, (2.16) is the output of the LPF. If it does not exist, then (2.16) is going to be equal to zero or almost zero, since the frequency $f - f_k$ is much larger than the cut-off frequency of the LPF. As observed in (2.16), accurate estimation of the DC components of both the positive- and negative-sequences of d and q components are essential for the spectral analysis, because the DC components include both the phase and amplitude information, which are A_k , B_k , and C_k ; and Φ_{A_k} , Φ_{B_k} , and Φ_{C_k} . Therefore, the smaller the phase delay of the LPF at zero frequency, the less error is achieved for the estimation of the spectral components of the EAF current. Low-pass filtering is achieved by ES in this research work. Since the amplitude of the fundamental component is much higher than the other frequency components, first the fundamental frequency component at 50Hz is

estimated and it is subtracted from the original current waveform, so that the remaining frequency components are estimated more accurately. Then parallel processing of the remaining waveform including the harmonics and the interharmonics is

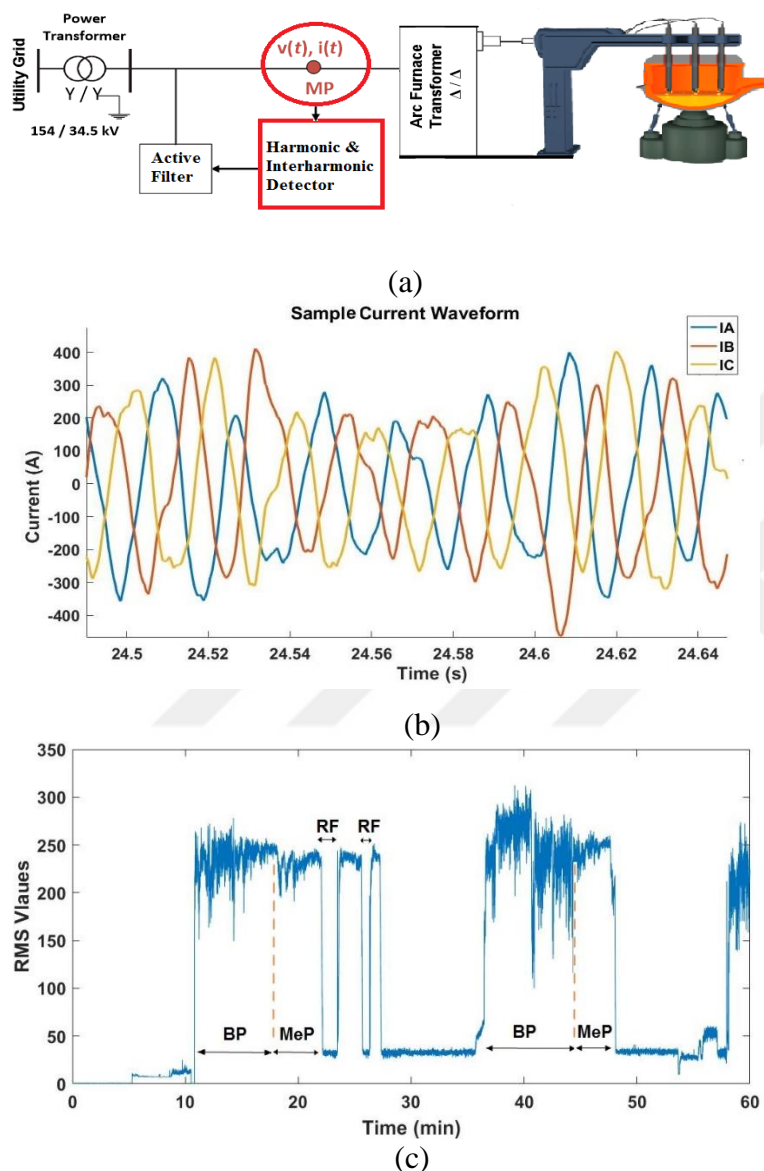


Figure 2.3. Obtaining the field data used in this research work; (a) schematic of the data collection at the measurement point (MP) and the proposed system, (b) sample three-phase current waveform obtained from the boring phase of the EAF current, (c) 10-cycle RMS of the EAF current for Phase-A for a period of 60min (BP: boring period, MeP: Melting Period, RP: Refining Period)

achieved using the same MSRF analysis with exponential smoothing. Figure 2.4. illustrates the overall system to obtain the fundamental and the other frequency components. The parallel processing is used to repeat the *Frequency Component Estimation Block* in Figure 2.4 for each harmonic and interharmonic frequency. In Figure 2.4, $T_{opt}(f)$ represents the

optimum order of exponential smoothing specific to the frequency, f . Obtaining the best order of the exponential smoothing method is described in detail in this subsection. In Figure 2.4, $i_{A, f}(T_{opt}(f), t)$, $i_{B, f}(T_{opt}(f), t)$, $i_{C, f}(T_{opt}(f), t)$ represent the output of the implemented system for each frequency component, f . For harmonics, f corresponds to the integer multiples of the fundamental frequency, while for the interharmonics, f corresponds to the integer multiples of 5Hz, which is the recommended frequency resolution in the IEC Standard for harmonic and interharmonic analysis [56]. In Figure 2.5, details of the estimation blocks (given in Figure 2.4) are illustrated. As given in Figure 2.5, both d and q components of the negative- and positive-sequences are obtained using MSRF analysis. Then exponential smoothing is applied to obtain their DC components. Next, back transformation is achieved to attain the current component at frequency f , which is also a function of the optimum order of exponential smoothing, $T_{opt}(f)$ for f . As the exponential smoothing order deviates from its optimal value, the estimation performance of the frequency component deteriorates.

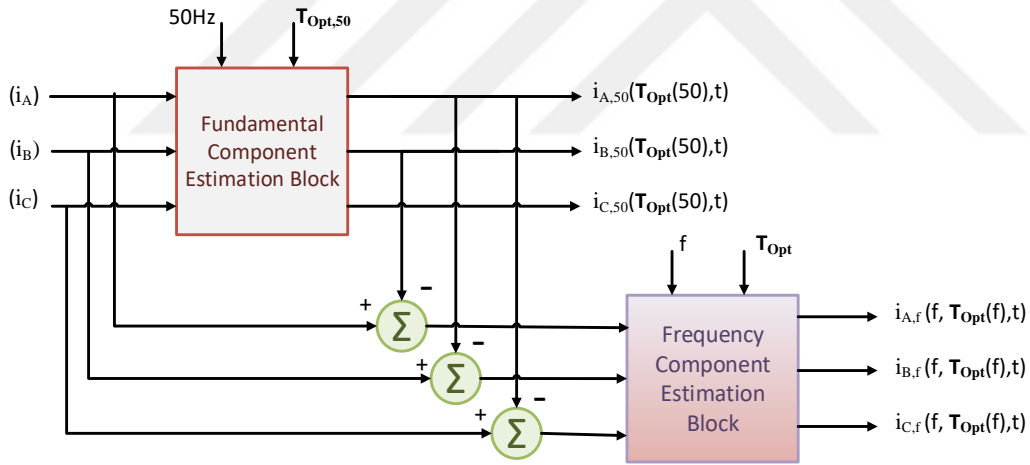


Figure 2.4. Extraction of the fundamental (50 Hz) component and the rest of all harmonic and interharmonic components

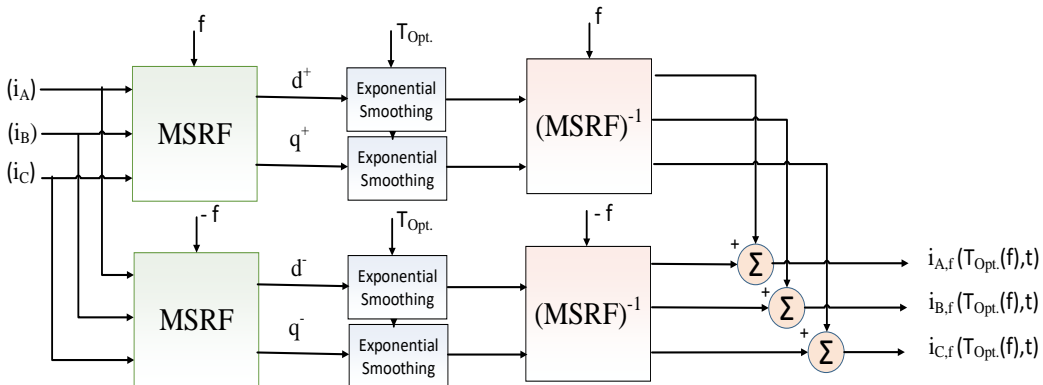


Figure 2.5. Frequency component estimation block: MSRF+ES application to obtain any frequency component

2.2.1. Exponential smoothing technique for low pass filtering

Exponential smoothing is used to estimate the DC variation of the data to obtain the low-pass filtered form of the positive- and negative-sequences of the d and q components of the frequency components. The input current waveform of the ES block is modeled as given in (2.17) according to [48]:

$$i(t) = a + bt + \varepsilon(t). \quad (2.17)$$

In (4), $a + bt$ is defined as the trend of the input waveform, which is required as the output of the ES block. The $\varepsilon(t)$ represents the variation around the trend of the current, which is required to be eliminated. The ES estimates the trend as the low-pass filtered form of its input given in (5):

$$i_{LPF}(t) = a + bt, \quad (2.18)$$

using the ES defined in [50] as in (6):

$$\hat{i}(n+1) = \sum_{n=0}^T (1-\beta)^n i(T-n). \quad (2.19)$$

T in (2.19) is the order of the ES operation, which is optimized per frequency component in this research work, $\beta = 0.333$ as suggested in [50], and n is the time index.

Obtaining the Optimal Exponential Smoothing Order for Each Frequency Component: Two criteria are used to obtain the optimum order for ES applied following the MSRF analysis: (i) Total Harmonic and Interharmonic Distortion (THID), (ii) Amplitude Error (AE) between the estimated frequency component and the corresponding frequency component of the original current waveform. A function of these two criteria is obtained for different orders of ES in order to obtain the optimum order matching each harmonic or interharmonic frequency component. Then obtaining the best matching order of ES for each frequency component can be solved as an optimization problem given in (2.20):

$$\left\{ \begin{array}{l} \min \left\{ \frac{1}{M} \sum_{k=1}^M \alpha \cdot THID_k(T(f)) + (1 - \alpha) AE_k(T(f)) \right\} \\ \text{subject to} \quad 10ms \leq T(f) \leq 40ms \end{array} \right\} \quad (2.20)$$

In (2.20), M represents the number of 10-cycle analysis windows, along which the THID and AE computations are carried on. M is taken to be 3000, which corresponds to 10-cycles inside 10-min period of the boring phase. $THID_k(T(f))$ is the THID computed for the k^{th} 10-cycle frame using ES order of T for the frequency component f . Similarly, $AE_k(T(f))$ is the amplitude error of the frequency component f with the order of T for ES. The range of $T(f)$ corresponds to the half cycle of the fundamental frequency to 20 cycles and the minimization is achieved by incrementing the $T(f)$ value from 10 ms to 400 ms with a step size of 10 ms. In (2.20), α determines the balance between the two criteria and it has been equated to 0.7 for the fundamental frequency and 0.6 for other frequency components. After all the minimization process is achieved for all frequency components from the fundamental frequency to the 50th harmonic with 5Hz resolution, $T_{opt}(f)$ is obtained.

Amplitude error (AE) is computed as the absolute error between the amplitudes of the component that is being extracted, using the 10-cycle Discrete Fourier Transform (DFT) of the original waveform and the 10-cycle DFT of the waveform including only the extracted frequency component, which is the output of the proposed MSRF+ES method. Therefore, AE is a measure of the accuracy of individual frequency component detection, while THID is the measure of the misdetection of the components other than the extracted component. A sample comparison for the spectrum around the fundamental component is given in Figure 2.6. In Figure 2.6 (a), (b), and (c), the original amplitudes (in blue) are compared with the DFT of the estimated fundamental current component by the proposed method for the ES order of 10 ms, 300 ms, and 140 ms, respectively. Figure 2.6 (d) shows the same comparison for the fundamental estimation using MSRF+KF algorithm, proposed previously in [7]. In Figure 2.7, block diagrams of the computation of the two criteria, which are AE and THID are given both for the fundamental frequency and other frequency components.

It is observed that for the comparatively small order of 10 ms in Figure 4(a), the fundamental component estimation is successful, however, the obtained $i_{A,f}(T_{opt}(f), t)$ still

includes other frequency components around the fundamental frequency, which are 40Hz, 45Hz, 55Hz, 60Hz, and etc, which results in high AE. For the much larger order of 300ms (Figure 2.6 (b)), the interharmonic frequency components are successfully eliminated, however, estimation of the fundamental component is not very accurate. In order to obtain the best order, the two criteria are applied on the DFTs of the original and the extracted waveform of the specific frequency component. THID computation is as given in (2.21):

$$THID_f = \frac{\sqrt{\sum_{i=0}^N G_{5i}^2 - G_f^2}}{\sqrt{\sum_{i=0}^N G_{5i}^2}} 100. \quad (2.21)$$

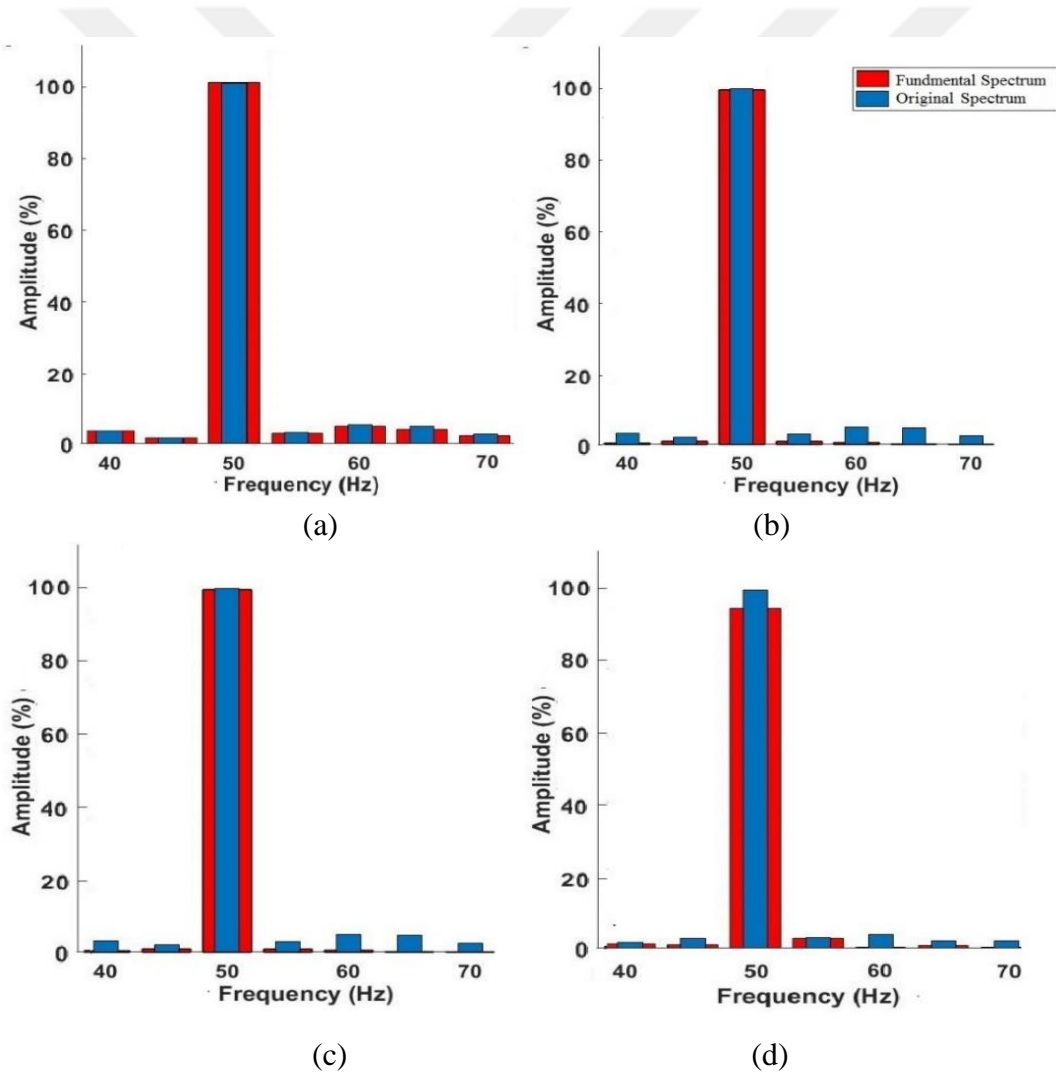


Figure 2.6. Comparison of the original EAF current spectrum (blue) with the extracted fundamental component spectrum using MSRF+ES (red) for exponential smoothing with an order of size (a) 10ms, (b) 300ms, (c) 140ms, which is the best in terms of fundamental estimation and low THID, and (d) using MSRF with Kalman filtering

In (8), $G5i$ represents the amplitudes of the frequency components with 5 Hz resolution based on 200-s DFT windows, whereas G_f stands for frequency component to be. In (2.21), N is the index of the 5-Hz-apart frequency components to be summed up. It can be concluded from both Figure 2.6 and Figure 6 that, small order of ES results in high THID and low fundamental AE, and large order of ES results in low THID and high AE. For the fundamental frequency component estimation using MSRF+ES method, order of 140 ms has been determined as the best order of ES application based on the two criteria. To clarify, the THIDs and AEs corresponding to different ES orders for the fundamental frequency and the interharmonics at 45Hz and 55Hz are given in Figs. 2.8 and 2.9, respectively. In order to obtain the optimal orders, THID and AE are computed for all frequency components and the optimal ES order is obtained using (7).

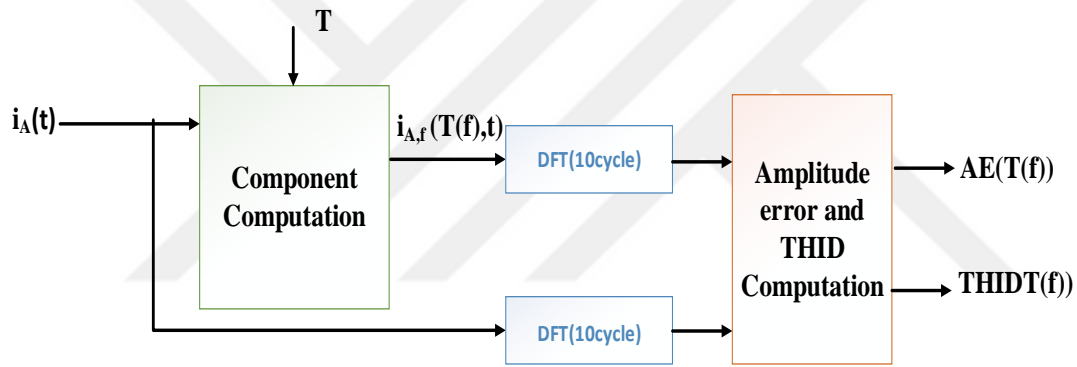


Figure 2.7. THID and amplitude error (AE) computation for any frequency component to obtain the best order of ES for each

The optimum orders ($T_{opt}(f)$) of MSRF+ES analysis obtained as the solution of the optimization problem defined in (2.20) for the most typical EAF boring phase harmonics and interharmonics are given in Figure 2.9.

It should be noted here that, the ES algorithm can also be used with a constant order for all harmonic and interharmonic frequencies, however, in order to obtain the shortest possible estimation delay, the presented optimization procedure is run over the 10-min boring phase data of the EAF current to make the best and fastest possible estimation. In fact, the algorithm will still work for any constant order ES without the optimization. For each measurement site, the train process may be run before starting the measurements and it can be repeated regularly for possible updates, and this procedure cannot be considered as a drawback of the proposed algorithm.

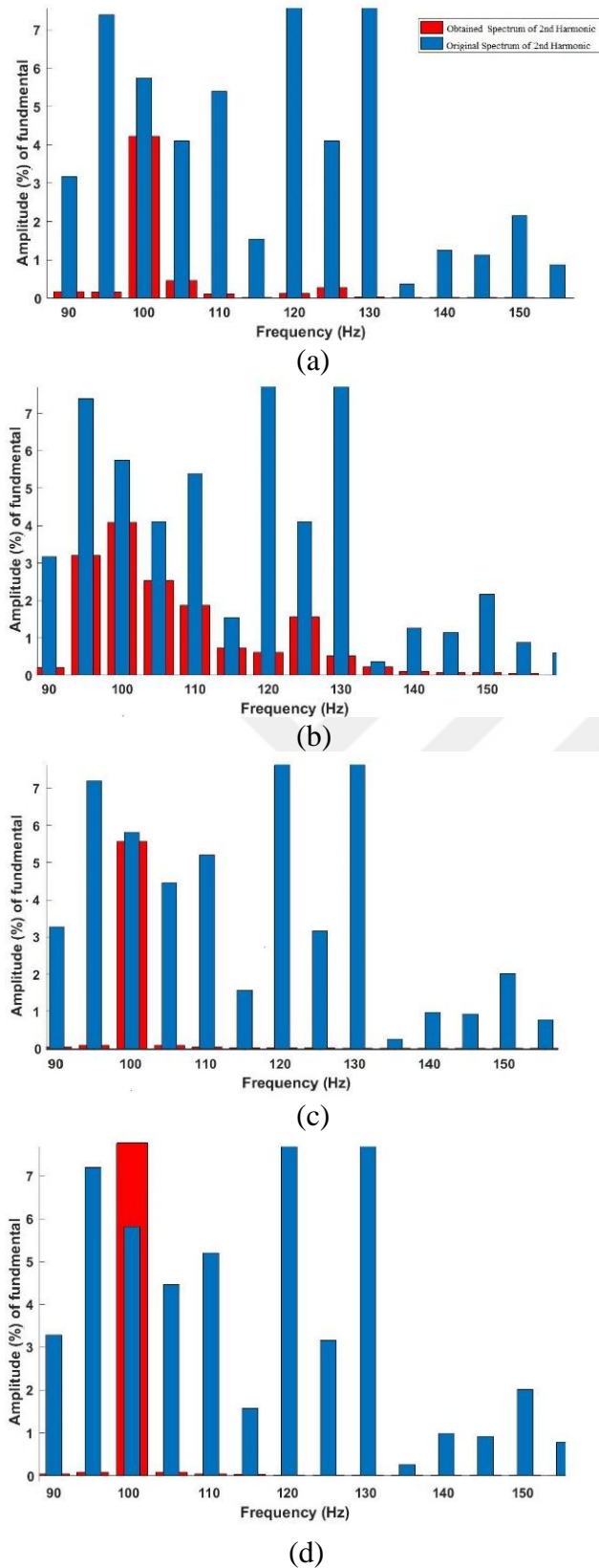


Figure 2.8. Comparison of the original EAF current spectrum (blue) with the extracted second harmonic component spectrum using MSRF+ES (red) for exponential smoothing with a order of (a) 160ms, (b) 10ms, (c) 80ms, which is the best in terms of fundamental estimation and low THID, (d) using MSRF with Kalman filtering

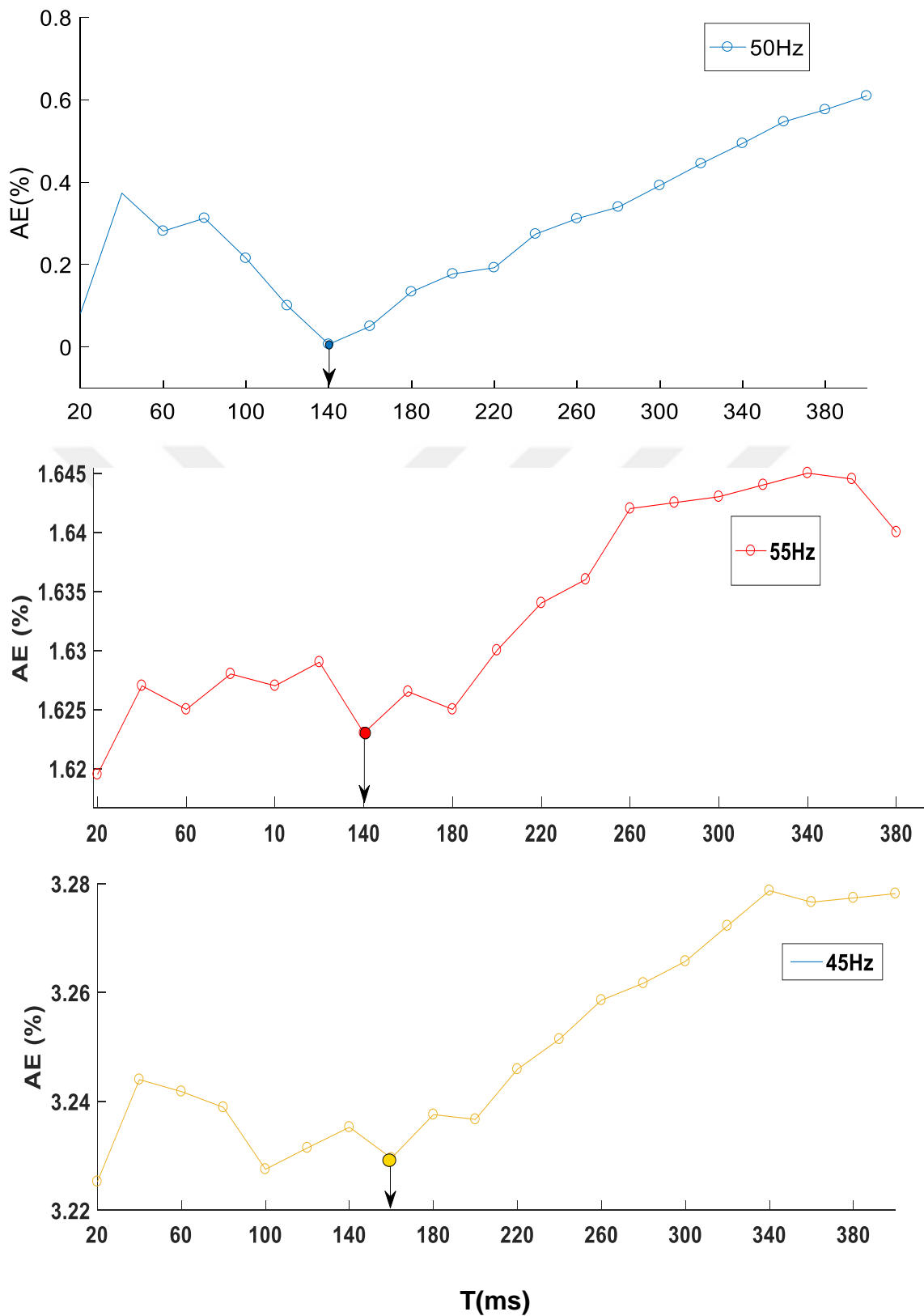


Figure 2.9. Amplitude error of the MSRF+ES estimation compared to the original waveform component with respect to ES order for the fundamental frequency (50Hz), and interharmonics at 45Hz and 55Hz. Error is computed for a typical boring phase period of 10-min cycles (mean error of 3000 10 cycles of the fundamental) as the percent of the original frequency component amplitude

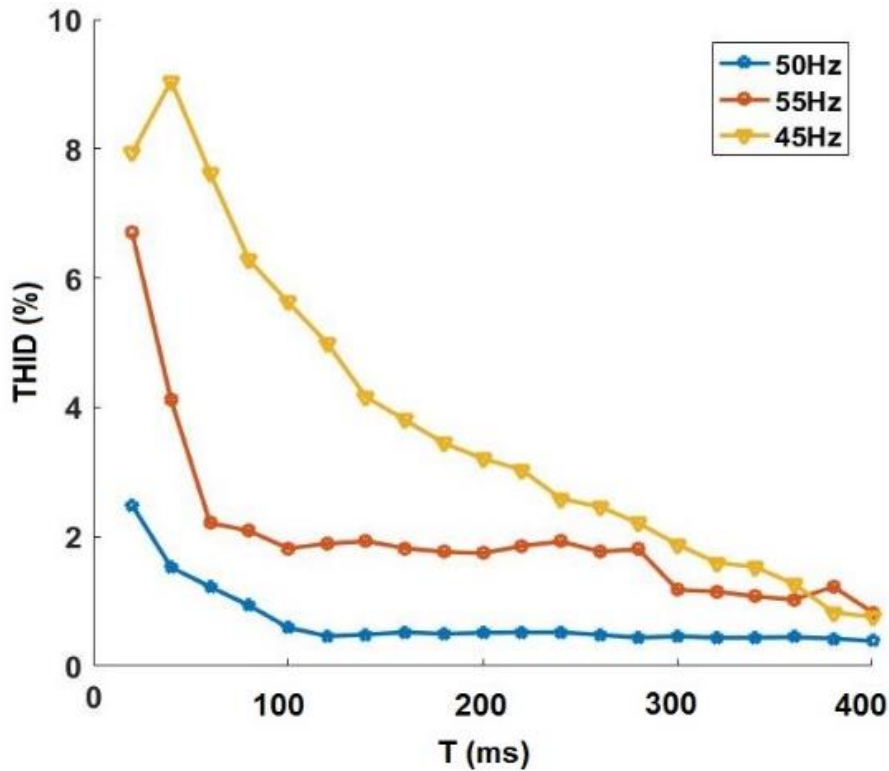


Figure 2.10. THID for the fundamental (50Hz) and interharmonics at 45Hz and 55Hz obtained from the MSRF+ES for a typical boring phase period of 10-min cycles (mean error of 3000 10 cycles of the fundamental)

2.3. Method Developed for Power Quality Event Classification

PQ event data used in this work is provided by the National Power Quality Monitoring System of Turkey, whose architecture is illustrated in Figure 2.12. [2]. The aim of the work presented in this research work is to use deep learning techniques to obtain a successful PQ event classification.

PQ events are defined as the voltage interruptions, voltage sags and voltage swells by the Standard IEC-61000-4-30 [1]. A swell event is detected when the root mean square (RMS) of the measured voltage exceeds the nominal RMS value by 10%, while a sag (dip) event is defined as the reduction of the RMS value of the voltage by more than 10%, and an interruption is defined to occur when the RMS value of the voltage is more than 90% less than its nominal RMS value and an interruption is known as the most serious event [1].

The data used in this research work, includes raw event data are collected for a period of one-year from four different regions of the electricity transmission system with 25.6KHz

sampling rate. Table 2.2 summarizes the information of the whole event data used in this work. The RMS value computation from raw voltage data is achieved every cycle of the 50Hz fundamental frequency of the power grid, which ideally corresponds to 20ms according to [1], so that they are transformed to form event matrices of sizes 3x150. Figure 2.13. (a) presents a real event data collected from the transmission system of Turkey using the architecture given in Figure 2.12. Each phase of the voltage is represented by a different color and the RMS values computed for each cycle (every 20ms) is given, hence 150 cycles represent 3s of voltage data. Here the nominal RMS value of the voltage is normalized to 100 Vrms, therefore it can be seen that there is a general reduction of the voltage, for the whole measurement period, however there are serious voltage sags in in phases *A* and *B* from approximately cycle 25th to 55th and voltage swell in Phase *C* during the same measurement period as shown in Figure 2.13. (a). The both the lengths and the amplitudes of the voltage sags, swells and interruptions may vary from event to event. Therefore, an event length may vary from a few samples in each window to the total length of the data, which is 3s in this case. Considering the different possible event amplitudes and the three phases of power system, may different event types may occur and they have to be classified so that automatic countermeasures for the power system can be generated in real-time for a smart grid.

For the purpose of analysis in this work, all three phases are arranged as a single voltage RMS vector as given in (2.22):

$$X_{Event} = [V_A[0] \dots V_A[149] \quad V_B[0] \dots V_B[149] \quad V_C[0] \dots V_C[149]]. \quad (2.22)$$

which is also shown in Figure 2.13 (b). *A*, *B* and *C* subscripts in (2.22), represent three phases and the RMS values of voltage data for each cycle in each phase is settled together with the other phases in a single 1x450 voltage RMS matrix as shown in Figure 2.13 (b). All 1337 events in Table 2.2 are plotted and saved in “.jpg” format. They are all manually labeled to form 10 groups of events and arranged inside 10 folders for the event types. The

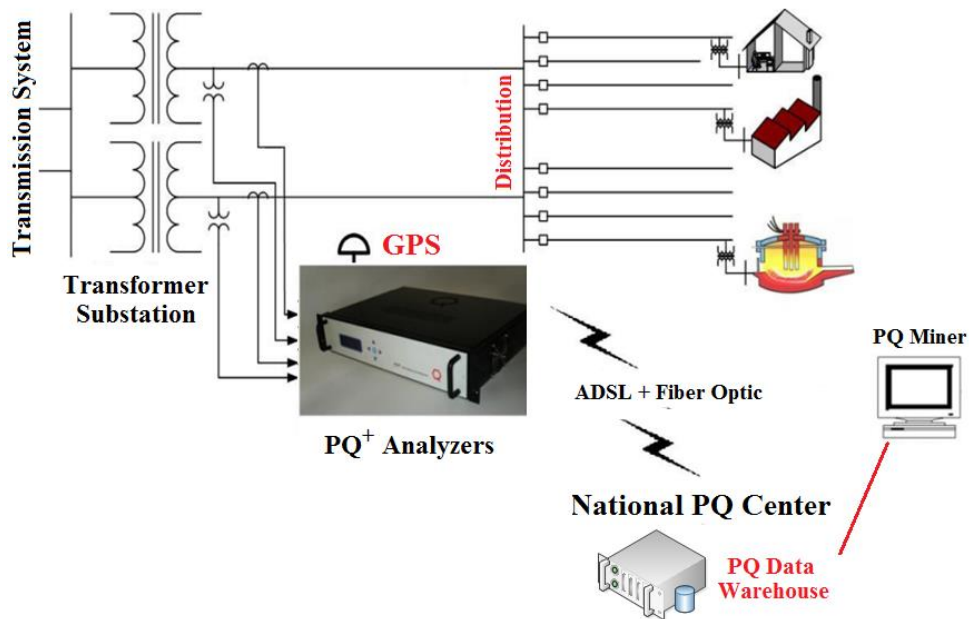


Figure 2.11. The PQ monitoring system architecture [2]

types of the events are listed in Table 2.3 85% of the whole event data is used for the train process of the MLCNN and 15% is used for the test. Cross validation is also applied to obtain the test results.

The aim of event classification using machine learning techniques is to achieve a deep understanding of PQ events – like a human data expert vision or even better- with machines.

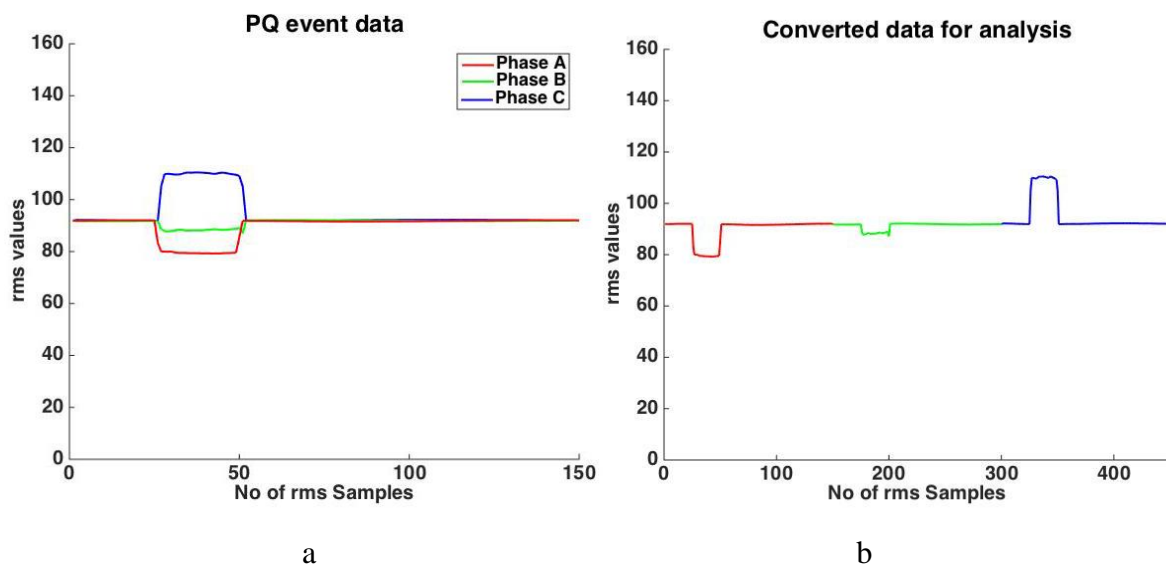


Figure 2.12. Sample sag event in two-phases and swell in the other phase, (a) RMS voltages of each phase, (b) arranged event data in a single row vector

Table 2.2. PQ event data obtained from the transmission system (1337 events in total)

Transformer Substation (TS)	Feeder id	Type	Event Number (per one-year)
TS1	3	Heavy Industry	353
TS2	33	Industry + Urban	216
TS3	53	Urban	746
TS4	4	Rural + Industry	103

Table 2.3. PQ event data labels obtained manually for all the events listed in

Event id	Event Type	Event Number (per one-year)
1	One sag and one swell in three phases	395
2	Long-sag in one phase	312
3	Instantaneous sag in three phases	240
4	Interruption in three phases	186
5	Interruption in one phase	99
6	Instantaneous-sag in one phase	66
7	Swell in one phase	30
8	Two interruptions and one sag in three phases	50
9	Interruption in two phases	20
10	Frequent and short interruptions in all phases	20

The number of event data used in this work is not high enough, but considering event data coming from all transformer substations from all over the transmission and distribution system, the number of events received at the PQ center every minute can be compared to the 150 hours of video uploaded every 60 seconds to the YouTube website [72]. Hence, there is no way for human ability to analyze such a big data. It is crystal clear that a proper way to understand such huge amount of data is one of the most important necessities and deep learning is known as the most up-to-date method for such analysis, which is defined as the first method of artificial intelligent technique that is able to see, listen, think and comment [65].

In this section, the approach of using deep neural networks for PQ event recognition and classification is described. Based on related reference works starting with LeNet-5, GoogleNet, ImageNet [67-71], Convolutional Neural Networks (CNN) generally have the same format – weighted convolutional layers (optionally followed by contrast normalization and max-pooling), which are tracked by one or more fully-connected layers. Figure 2.14. is an example of Classification with Deep CNN from ImageNet [67]. Details of the layer formation in Figure 2.15. are given in the following section.

2.2.2. Architecture overview

A standard NN gets a single vector as input and by having fully connection of all neurons to the previous layer, and neurons with an independent single layer function, it provides classification class scores called weights (w) as illustrated in Figure 2.15. (a). For instance, for an image sized $32 \times 32 \times 3$, a single NN hidden layer has $32 \times 32 \times 3 = 3072$ weights. This amount of weights seems manageable but when the size of data gets bigger like $200 \times 200 \times 3$, 120,000 weights would be obtained in the first layer. In other words, NNs receive an input (a single vector), and transform it through a series of hidden layers. Each hidden layer is made up of a set of neurons, where each neuron is fully connected to all neurons in the previous layer, and where neurons in a single layer function completely independently and do not share any connections. The last fully-connected layer is called the “output layer” and in classification settings it represents the class scores. Thus, to get free from overfitting problems and quickly adding up, the MLCNN is employed as the deep learning method in this research work. CNNs take advantage of the fact that the input consists of images and they constrain the architecture in a more sensible way. In particular, unlike a regular NN, the layers of a ConvNet have neurons arranged in three dimensions: width, height, depth. (Note that the word *depth* here refers to the third dimension of an activation volume, not to the depth of a full NN, which can refer to the total number of layers in a network.) For example, the input images in $32 \times 32 \times 3$ with are an input volume of activations, and the volume has dimensions $32 \times 32 \times 3$ (width, height, depth respectively). As we will soon see, the neurons in a layer will only be connected to a small region of the layer before it, instead of all of the neurons in a fully-connected manner which is illustrated in Figure 2.15 (b).

Two most important functions that are mostly used in the MLCNN are Convolution and MaxPooling. Brief definitions for these functions are given below:

- *Convolution* first multiplies the selected weight values with the data and then sums all of them. Then it shifts the weight window on the data image with the optional amount like one or two.

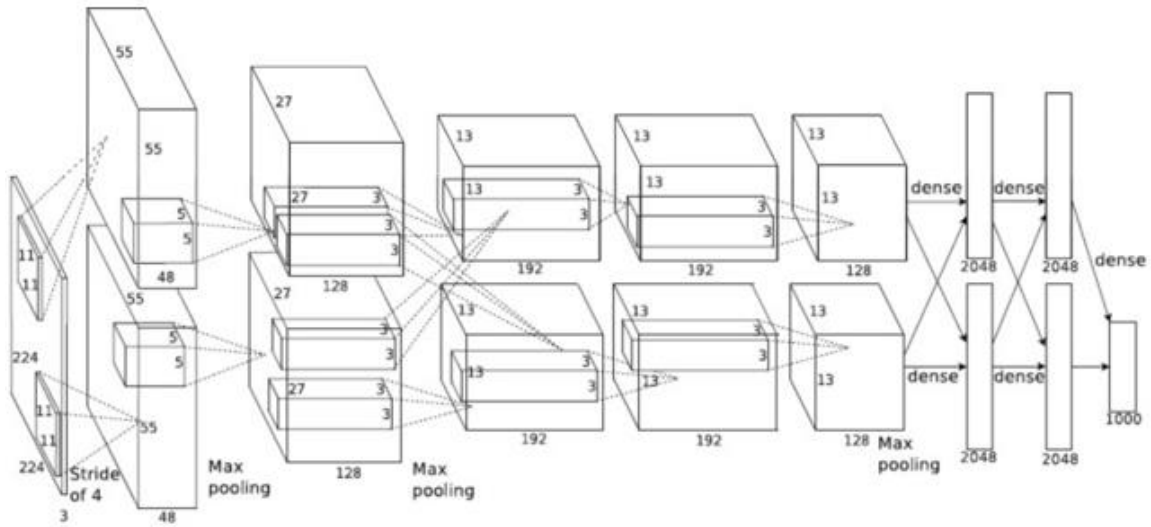


Figure 2.13. Image net classification with deep convolutional neural networks [16]

Figure 2.16 (a) is a demo of a CONV layer. Since 3D volumes are hard to visualize, all the volumes (the input volume (in blue), the weight volumes (in red), the output volume (in green)) are visualized with each depth slice stacked in rows. The input volume is of size $W_I=5, H_I=5, D_I=3$ and the CONV layer parameters are $K=2, F=3, S=2, P=1$. That is, we have two filters of size $3 \times 3 \times 3$, and they are applied with a stride of 2. Therefore, the output volume size has spatial size $(5 - 3 + 2)/2 + 1 = 3$. Moreover, notice that a padding of $P=1$ is applied to the input volume, making the outer border of the input volume zero. The visualization below iterates over the output activations (green), and shows that each element is computed by elementwise multiplying the highlighted input (blue) with the filter (red), summing it up, and then offsetting the result by the bias.

MaxPooling is a function which downsamples the available matrixes. Figure 2.16 (b) is an example of using this function. In Figure 2.16 (b), assume that Y is a matrix, which is obtained after convolution. A 2×2 MaxPool filter gets the maximum value of Y from every 2×2 matrix indexes.

From the input image data matrix, after Convolve and MaxPool operations, a $1 \times 1 \times 10$ score vector is obtained for 10 classes of images or any other data and this is the aim that MLCNN is trying to achieve. So that with the full size image data is reduced into a single vector of class scores, arranged along the depth dimension.

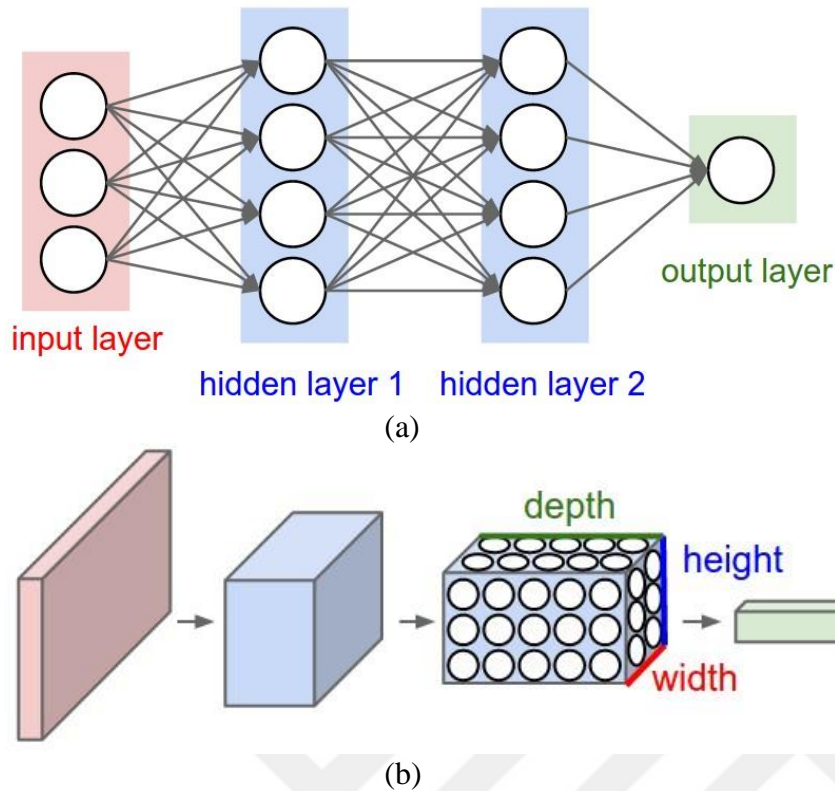


Figure 2.14. Layer structure of a (a) NN, (b) MLCNN

Deep learning architecture used for PQ event image data classification is given in Figure 6. For the deep learning application on image data, DIGITS (the Deep Learning GPU Training System) application environment of NVIDIA has been employed[71]. The fundamental steps of the MLCNN method can be summarized as INPUT, CONV, RELU, NORM, POOL, and FC as shown in Figure 2.17. Below given are the explanations for each step:

- An event raw data as an INPUT $[220 \times 220 \times 3]$ holds the raw pixel values of the image, in this case an image of width 220, height 220, and with three color channels R, G, B.
- In CONV layer the output of neurons that are connected to local areas in the input is computed. These computed elements are produced between input and final weights. As an example if we try to use 12 filters the obtained matrix becomes $[220 \times 220 \times 12]$.
- The elementwise activation will be applied with RELU layer function. The actions like $\max(0, x)$ thresholding at zero. This function leaves the other layers output unchanged ($[220 \times 220 \times 12]$) in terms of size. Figure 5(b) represents how the POOL function works on an example.
- Down-sampling process is performed by the POOL function. With down-sampling operation on any previous resultant, volume will be changed to $[110 \times 110 \times 12]$.

- NORM function represents normalization of the obtained weight scores after each convolution.

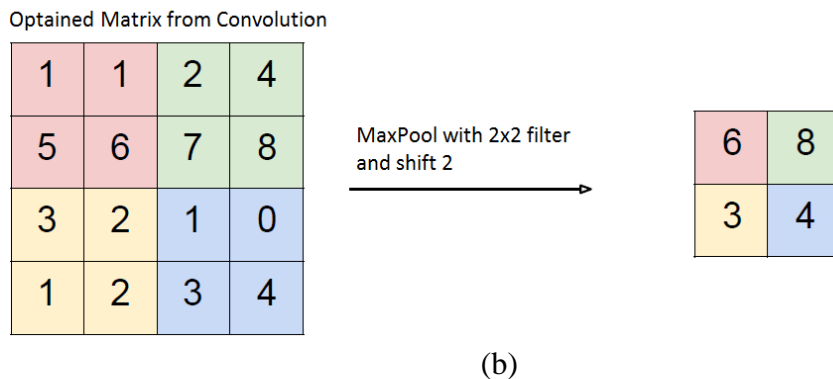
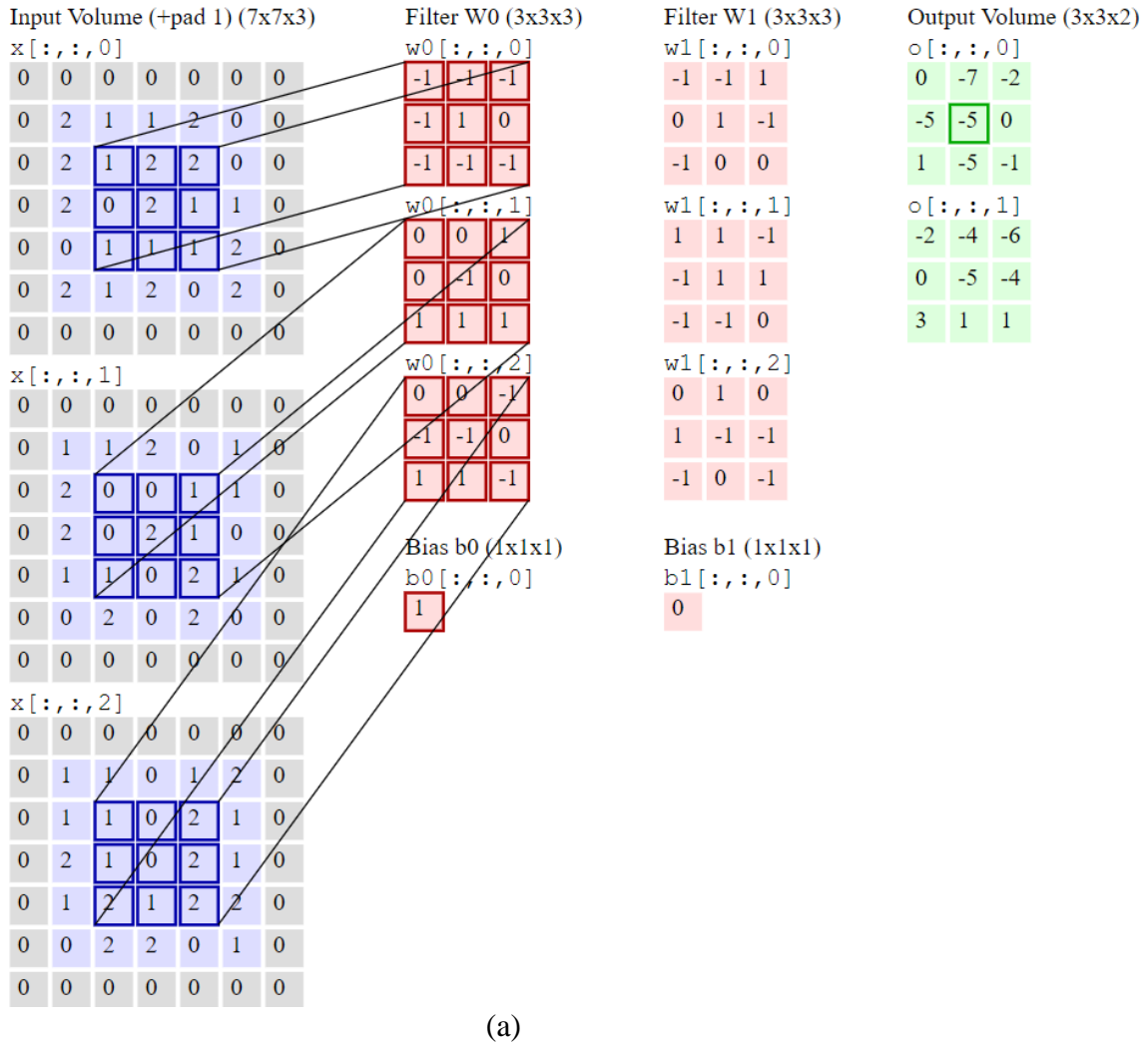


Figure 2.15. Examples: (a) first two steps of the convolving procedure for a 7x7 data matrix by a 3x3 weighting matrix, (b) application of MaxPool function with a 2x2 filter with two units of shifting

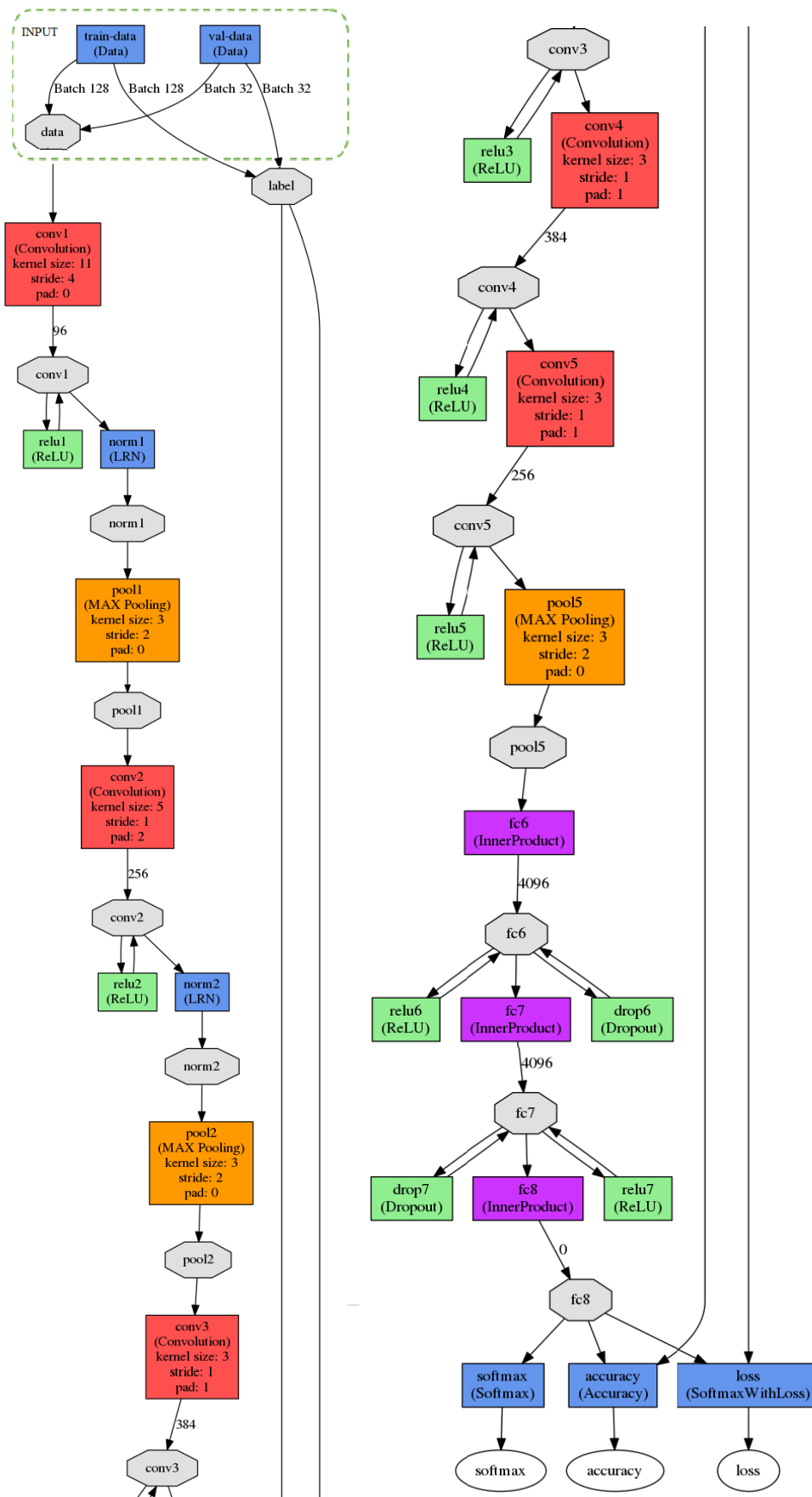


Figure 2.16. Flow chart of the implemented deep learning algorithm in this work, obtained by DIGITS deep learning application platform

In this case the number of classes is 10 therefore class scores will be obtained in a $[1 \times 1 \times 10]$ data vector. This vector is results in the final FC (fully-connected) layer. Applying the flowchart shown in Figure 2.16 on the PQ event data, softmax classifier, accuracy and loss are obtained. Discussion and explanations about these results are given in the next section.



3. RESULTS AND DISCUSSION

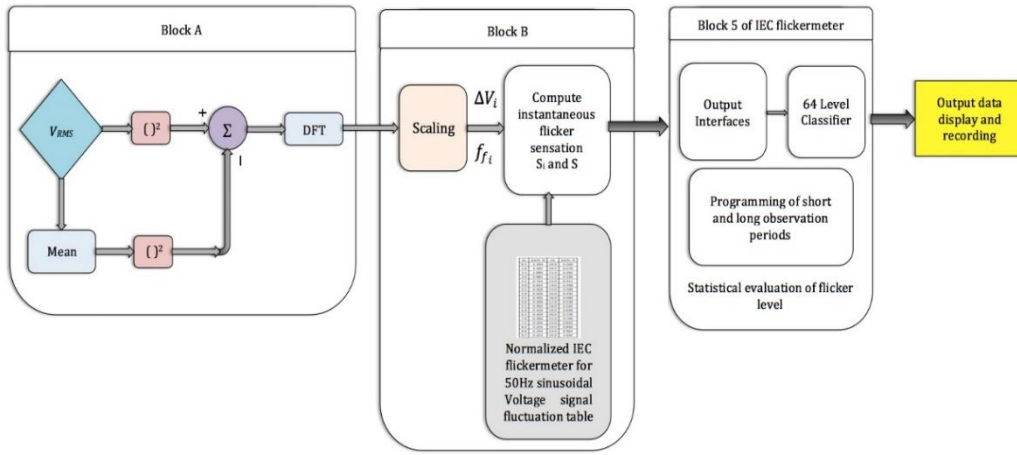
In this section results obtained from proposed methods will be presented in three subsections. The first subsection contains results from estimation of flicker component extracted from true rms values. Then the second subsection will address the results of real time detection of harmonics and interharmonics from current waveform. In third subsection results of developed deep learning based method for classification of PQ events will be addressed. Finally, a discussion will be done on the obtained results.

3.1. Results for Flickermeter

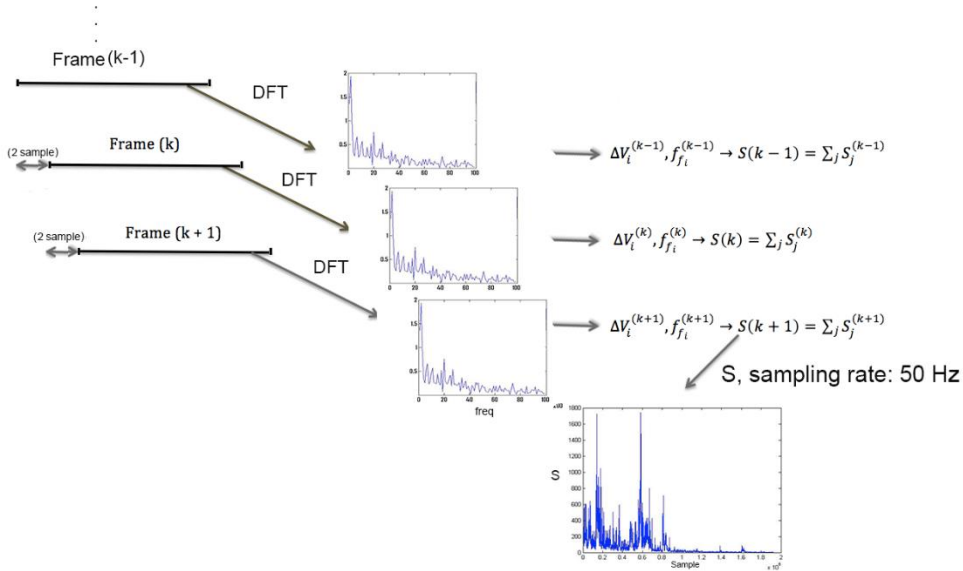
To verify the proposed method, the signal modelled as given in Section 2, has been generated for different f_{fi} and ΔV_i values and then the mean values of the flicker sensation, S , generated for 10-min period, has been obtained both by the IEC flickermeter and by the proposed method. Figure 3.1 illustrates the proposed digital realization of the proposed flickermeter using RMS of the voltage waveform. Figure 3.1 (a) is the general block diagram and Figure 3.1 (b) is the details of the signal processing in Block-A and Block-B. the results obtained from proposed method will be addressed in this subsection.

3.1.1. Verification of the proposed method using synthetic voltage waveforms

IEC flickermeter computes S values directly from the generated voltage waveform, while the proposed method assumes only the half-cycle RMS values of the voltage signal exists and computes S values using those RMS values. The results are given in Table 3.1., In the first three rows in Table 3.1 the expected value of the mean S is unity since $\Delta V/V$ and the corresponding flicker frequency values from Table 2.1 are used for the single flicker frequency component. Note that, as mentioned before in Section 3, Table 2.1 lists the flicker frequency and the corresponding amplitude values which result in unity instantaneous flicker sensation, S , at the output of Block-4 of the IEC flickermeter according to the IEC Flickermeter Standard [2].



(a)



(b)

Figure 3.1. Digital realization of the proposed flickermeter using RMS of the voltage waveform, a) The general block diagram, b) Details of the signal processing in Block-A and Block-B

It is shown that the proposed method successfully yields S values very close to unity. Similarly, for the other cases, where more than one flicker frequency component with various amplitudes given in Table 3.1 the mean values of the flicker sensation values are very close to those obtained by the digital realization of the standard IEC flickermeter. For the first five synthetic voltage waveforms in Table 3.1 (first five rows), the expected values of the mean values of S can be deduced directly from the input voltage waveform directly, which are given in the second row of Table 3.1. For a single flicker component mean of S should be unity, while it is expected to be two for two flicker components selected from

Table 2.1 [2]. The error rates for both the digital realization of the IEC flickermeter and the proposed method are given together with the mean S values in Table 3.1. It is observed that the proposed method generated instantaneous flicker sensation values with an error rate less than or equal to 0.04% in all cases and that is 0.099% for the digital realisation of the IEC flickermeter. The average error rate is obtained as 0.021% for the proposed method, while it is 0.045% for digital realisation of the IEC flickermeter for first five cases experimented in Table 3.1. From the S values computed by both the IEC flickermeter and the proposed method for a period of 10 minutes, flicker severity, P_{st} , has also been

Table 3.1. Mean of flicker sensation (S) values obtained by the proposed method using signal RMS values and by the IEC flickermeter using voltage waveform

Flicker Frequency Components and Corresponding Amplitudes	Mean (S) Expected Value	Mean (S)/ Error (%) Digital Realisation of the IEC flickermeter	Mean(S)/ Error (%) Proposed Method	P_{st} Digital Realisation of the IEC flickermeter	P_{st} Proposed Method
$f_{f1}=3.5\text{Hz}$, $\Delta V = 0.568$	1.0	0.9010/ 0.0990	1.0044/ 0.0044	0.6908	0.7001
$f_{f1}=8.8\text{Hz}$, $\Delta V = 0.25$	1.0	1.0073/ 0.0073	0.9906/ 0.0094	0.7041	0.7140
$f_{f1}=15\text{Hz}$, $\Delta V = 0.432$	1.0	0.9921/ 0.0079	0.9606/ 0.0394	0.6986	0.6901
$f_{f1}=3.5\text{Hz}$, $\Delta V_1 = 0.568$ $f_{f2}=8.8\text{Hz}$, $\Delta V_2 = 0.25$	2.0	1.9079/ 0.0461	1.9897/ 0.0103	0.9180	0.9300
$f_{f1}=8.8\text{Hz}$, $\Delta V_1 = 0.25$ $f_{f2}=16\text{Hz}$, $\Delta V_2 = 0.48$	2.0	1.9812/ 0.0094	1.9592/ 0.0408	0.9010	0.8919
$f_{f1}=8.8\text{Hz}$, $\Delta V_1 = 2 \times 0.25$ $f_{f2}=16\text{Hz}$ $\Delta V_2 = 2 \times 0.480$		7.9242	7.8370	1.550	1.4490
$f_{f1}=3.5\text{Hz}$, $\Delta V_1 = 0.568 \times 2$ $f_{f2}=8.8\text{Hz}$, $\Delta V_2 = 0.250 \times 2$ $f_{f3}=14\text{Hz}$ $\Delta V_3 = 0.388 \times 3$		13.8959	13.86	1.6950	1.7733

computed using Block-5 of the IEC flickermeter. The results are given in the last two columns of Table 3.1. It is observed that the proposed method also provides flicker severities very close to those generated by the IEC flickermeter. Hence, it can be concluded that the proposed method can successfully generate both flicker sensation and flicker severity from the half-cycle RMS values of a voltage waveform.

3.1.2. Verification of the proposed method using field data

For the verification using field data, a three-phase voltage waveform, sampled at a frequency of 3.2 kHz, collected from a transformer substation supplying one of the major electric arc furnace (EAF) installations of the country using the power quality monitoring systems developed through the National Power Quality Project of Turkey [16-17], has been used. RMS values computed every half-cycle from the voltage waveform are shown in Figure 3.2 for the three-phase 10-min voltage waveforms. The data is from the boring phase of the electric arc furnace operation; therefore, voltage waveform is dramatically time-varying as observed from Figure 3.3 Instantaneous flicker sensation, S , is computed by both the digital realization of the IEC flickermeter and the proposed method, for the 10-min measurement period and the mean values of S are compared in Table 3.2. S values for the 10-min period are also shown in Figure 3.3 to compare the responses of the IEC flickermeter and the proposed method. Flicker severity (P_{st}) values are also obtained from the 10-min S and the results are given in Table 3.3 for all three phases of the power system separately. It has been shown that the proposed method gives very close mean flicker sensation (S) and flicker severity (P_{st}) results with that of the mean values of the flicker sensation. The difference between the results obtained by the digital realisation of the IEC flickermeter and the proposed method is computed as the percentage of the value computed by the IEC flickermeter table given in [2] As given in the third and the sixth columns of Table 3.2, percentage differences are negligibly small, i.e. less than 0.01% for the mean of S and 0.4% for the P_{st} values.

Although flicker severity denoted by P_{st} is defined for only the 10-min measurement period, flicker severity can also be obtained out of instantaneous flicker sensation, S , values computed for 1-min, 5-min, and 15-min period according to the IEC Standard 61000-4-15 [2]. The comparison of the proposed method and the digital realisation of the IEC flickermeter is given in Table 3.3 for the 1-min flicker severity outputs. It can be concluded

from both Table 3.2 and Table 3.3 that the proposed method provides results very close to the IEC flickermeter results.

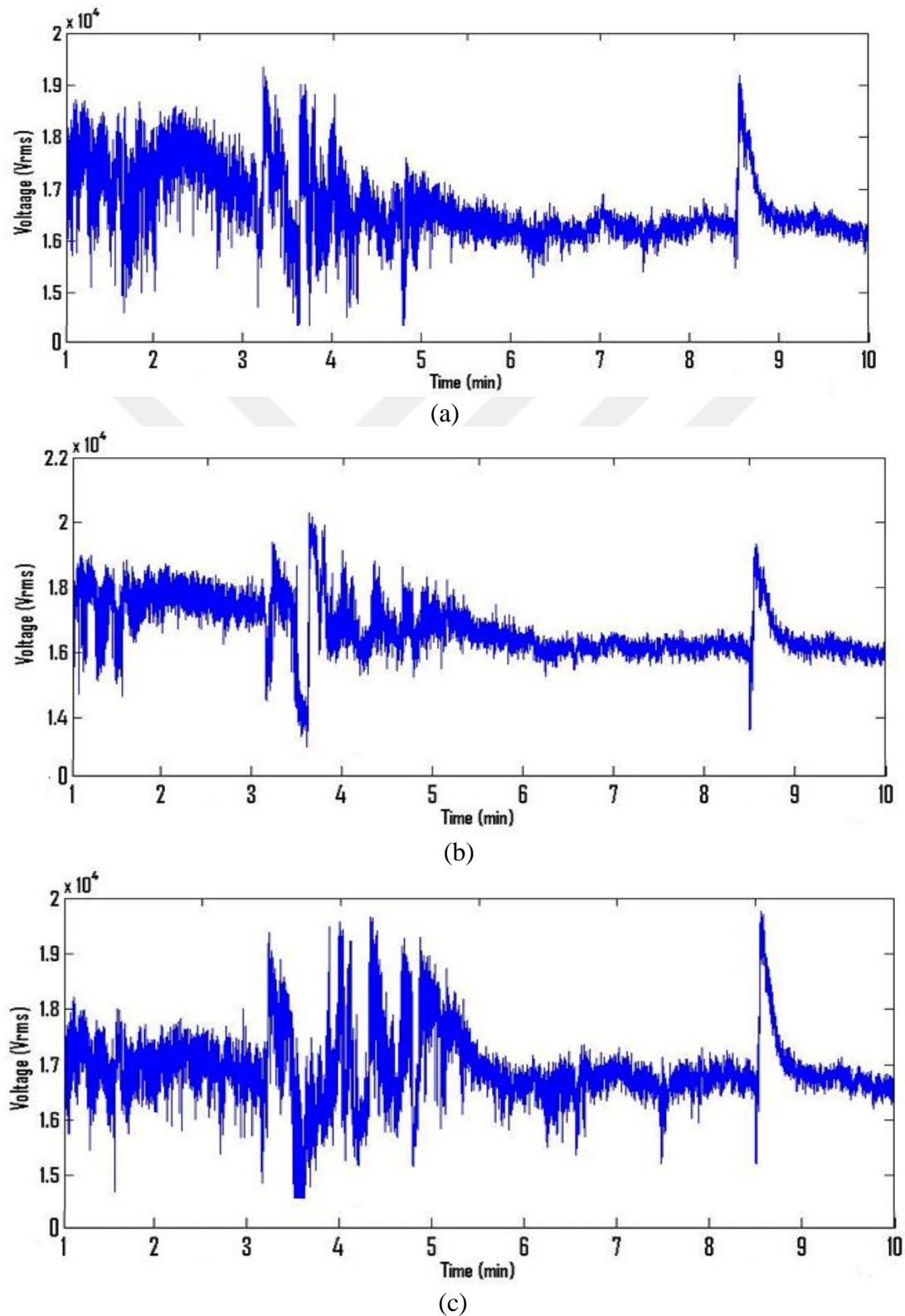


Figure 3.2. Half-cycle RMS of the three-phase voltage waveforms obtained from a transformer substation supplying an EAF plant, a) Phase-A, b) Phase-B, c) Phase-C

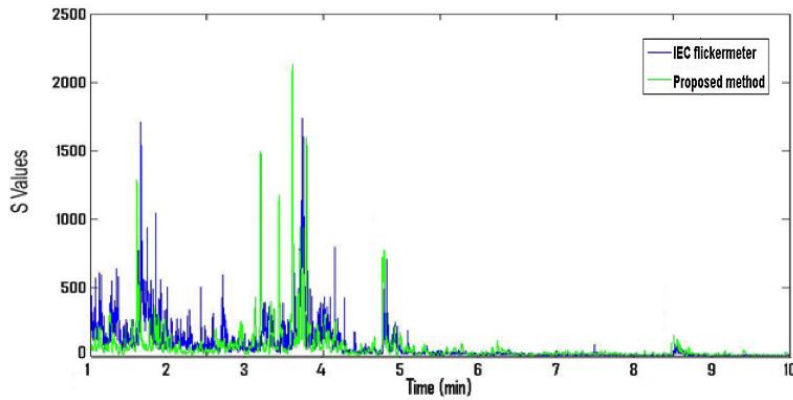


Figure 3.3. Instantaneous flicker sensation values, S , obtained by the digital realisation of the IEC flickermeter (blue) and the proposed method (green) corresponding to a voltage data of 10 minutes obtained from a transformer substation supplying an EAF plant

Table 3.2. Mean of instantaneous flicker sensation, S , values and the flicker severity, P_{st} , obtained by the standard IEC flickermeter and the proposed method (PM) from field data (10-min voltages obtained at a transformer substation supplying an EAF plant)

	Mean (S) IEC flickermeter	Mean(S) PM	Difference (%) (IEC& PM)	Pst IEC flickermeter	Pst PM	Difference, (%) (IEC & PM)
Phase A	72.85	72.78	0.0014	12.63	12.41	0.1352
Phase B	73.41	73.79	0.0071	11.36	11.54	0.1456
Phase C	71.36	71.84	0.0093	12.27	12.87	0.3965

Table 3.3. Comparison of the flicker severities obtained by the IEC flickermeter and the proposed method (PM)

Measurement Period (min)	Flicker Severity IEC flickermeter	Flicker Severity PM
(0-1)	15.93	15.54
(1-2)	10.06	9.84
(2-3)	11.80	11.45
(3-4)	16.34	16.86
(4-5)	10.25	10.21
(5-6)	3.53	3.53
(6-7)	2.76	2.71
(7-8)	3.02	2.99
(8-9)	3.79	3.79
(9-10)	1.82	1.85

3.2. Results and Discussion on Real Time Detection of Harmonics and Interharmonics

In order to compare the results of MSRF+ES with those of the MSRF+KF, the outputs of the two filters for the same input positive-sequence d component of the fundamental

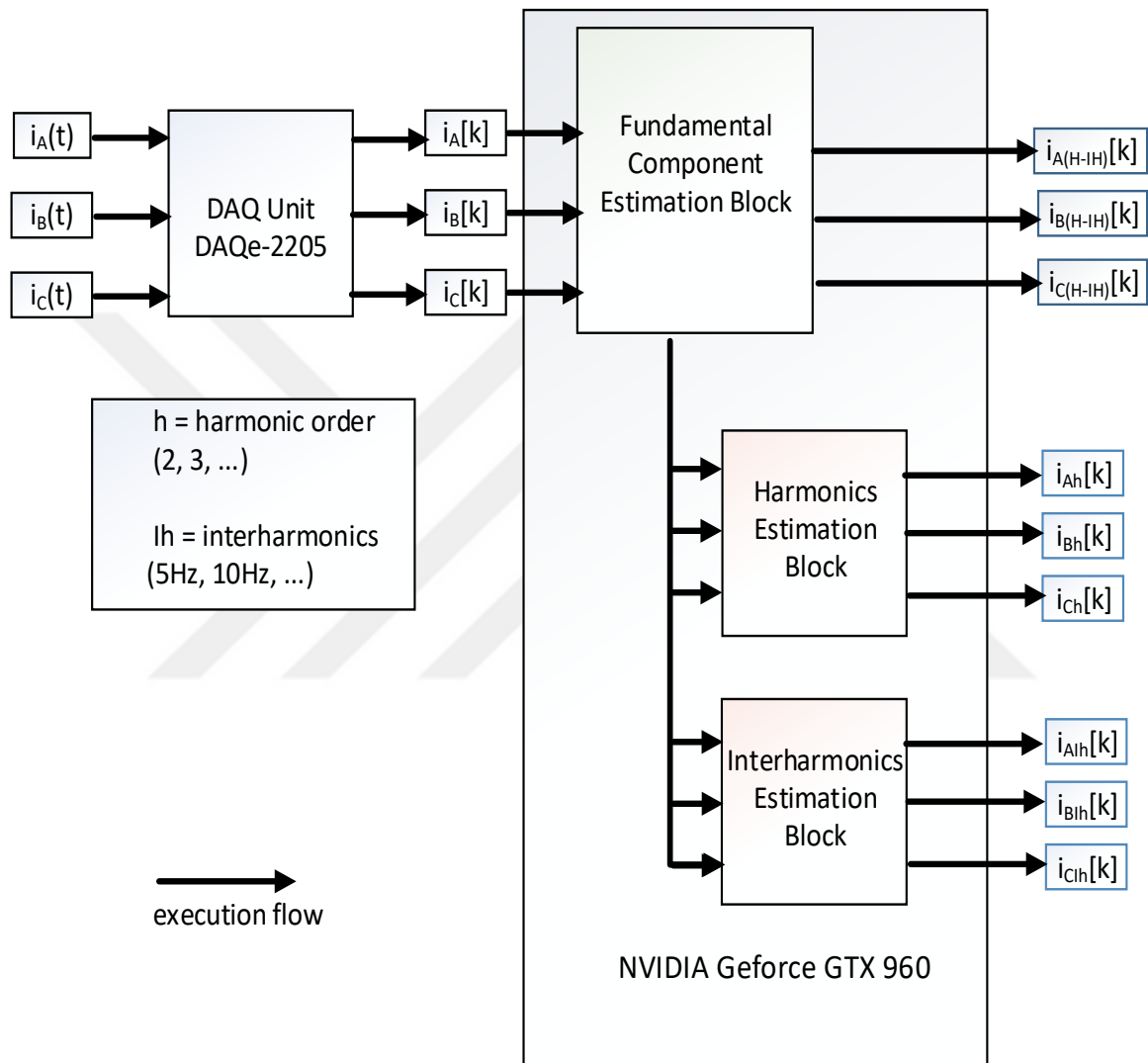


Figure 3.4. Block diagram of the GPU-accelerated MSRF+ES method implemented on NVIDIA Geforce GTX 960 graphics card

frequency is shown for a period of 45s in Figure 3.5 It can be concluded that for the whole measurement period, ES is preceding the KF output by a period of approximately $\Delta t=3\text{ms}$. The same observation has been also obtained for the negative-sequence d component and the positive- and negative-sequence q components. This situation increases the accuracy of both the amplitude and the phase estimations of all frequency components for MSRF+ES application.

The proposed MSRF+ES method to obtain the time-varying harmonics and interharmonics of the EAF currents is implemented on the GPU framework of a laptop computer. The three-phase EAF current waveform samples are obtained by the PQ analyzers developed through the National Power Quality Project of Turkey [56]. The 25.6kHz-sampled current

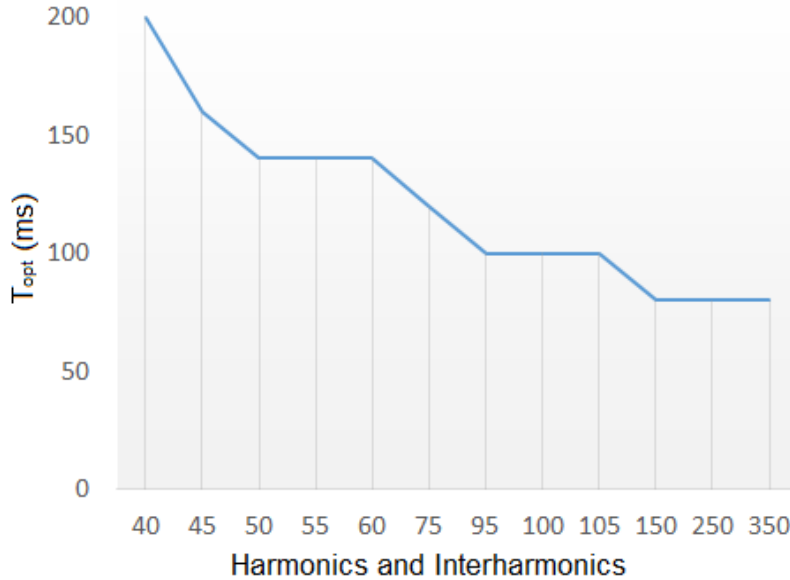


Figure 3.5. The optimum orders ($T_{opt}(f)$) of MSRF+ES analysis obtained as the solution of the optimization problem defined in (2.20) for the most typical EAF boring phase harmonics and interharmonics

waveforms are then used to obtain the fundamental frequency component, harmonics up to 50th harmonic and all interharmonics at the integer multiples of 5Hz resolution as recommended in [56]. The use of GPU lets the parallel processing of all interharmonics and harmonics, significantly reducing the data processing duration and making the analysis real-time. The processing durations of one-min three-phase EAF current data per frequency component is given in Table 3.4. The comparison in Table 3.4 is achieved for the three cases, application of MSRF+ES without GPU, MSRF+KF without GPU, and finally MSRF+ES implemented on NVIDIA Geforce GTX 960 graphics card (with GPU). In Table 3.4, processing duration per data sample is also provided. For the sampling rate of 25.6kHz, the time between two subsequent samples is $39\mu\text{s}$, therefore, if the processing time per sample is less than $39\mu\text{s}$, for all the harmonics and interharmonics, then it can be concluded that real-time operation is possible. Also note that, durations in Table 3.4 are per frequency component, hence the processing durations will be directly multiplied by the number of frequency components to be estimated, for the cases without GPU. According to

the execution flow in Figure 3.4 for the case of GPU use, it has been shown that the total processing duration of one-min data of the fundamental, harmonics and interharmonics up to 50th harmonics, is reduced to 2.5 s, which makes real-time operation of harmonics and interharmonics analysis serve the needs of any active power filtering application. However,

Table 3.4. Processing times of one-min EAF current data for MSRF+ES, and MSRF+KF on CPU, and MSRF+ES implemented on NVIDIA geforce GTX 960 graphics card (GPU)

	MSRF+ES (no GPU)	MSRF+KF (no GPU)	MSRF+ES (with GPU)
Time to process one-min data for a single frequency component	45s	75s	1.5s
Time to process one-min data for a single frequency component per sample	48.07 μ s	480.76 μ s	0.9615 μ s

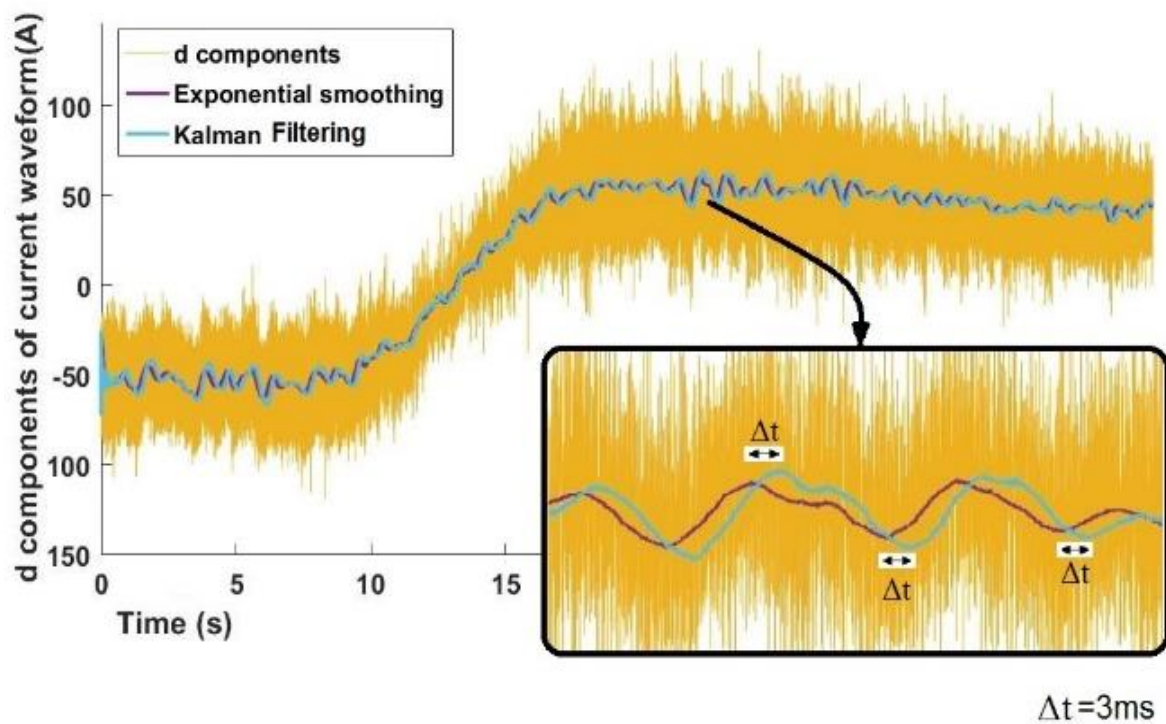


Figure 3.6. Positive sequence d component for the fundamental frequency together with its DC component obtained by Kalman Filter and ES

for MSRF+KF and MSRF+ES without using GPU, the processing durations, which are determined as the number of frequency components to be analyzed multiplied by the processing durations shown in Table 3.4, are obviously not suitable for real-time operation. To compare the estimation accuracy of both the phases and amplitudes of the fundamental frequency component and all harmonics and interharmonics, the current waveform is

reconstructed out of its MSRF+ES estimated components with optimal orders (fundamental, harmonics at 2nd and odd ones up to 30th, and interharmonics with 5 Hz resolution up to 150Hz). The result is shown together with the original waveform in Figure 3.6 for the phase-A current of the EAF.

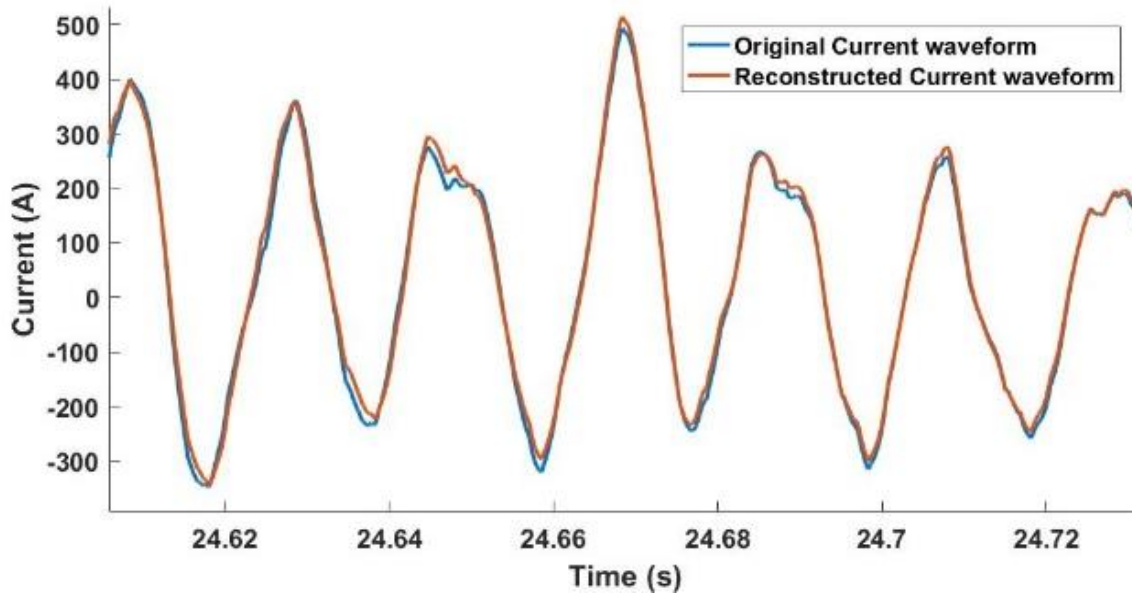


Figure 3.7. Comparison of the original EAF current with the reconstructed EAF current waveform, constructed by summing up the estimated frequency components with MSRF+ES method (fundamental, harmonics at 2nd and odd ones up to 30th, and interharmonics with 5 Hz resolution up to 150Hz)

Moreover, in order to observe the performance of any possible APF application, some frequency components estimated through MSRF+ES with the optimal ES orders are subtracted directly from the original current waveform. In Figure 3.7 (a), the estimated time domain components at 100Hz, 105Hz, and 95Hz are subtracted from the original current waveform and their 10-cycle DFT's are compared around 100Hz. It is observed that the proposed MSRF+ES method is good at eliminating the second harmonic subgroup defined in [56]. For the elimination of the interharmonics around the fundamental, which are usually high and rapidly fluctuating for the EAF currents, the interharmonic components at 30Hz, 55Hz, 60Hz, and 65 Hz are subtracted from the original waveform and the comparison of the 10-cycle DFT with the original waveform spectrum is given in Figure 3.7 (b). Note that the selected interharmonic components are those with the highest amplitudes around the fundamental. It is observed that the proposed method is successful at estimating the interharmonic amplitudes and phases accurately as observed in Figure 3.7 (b).

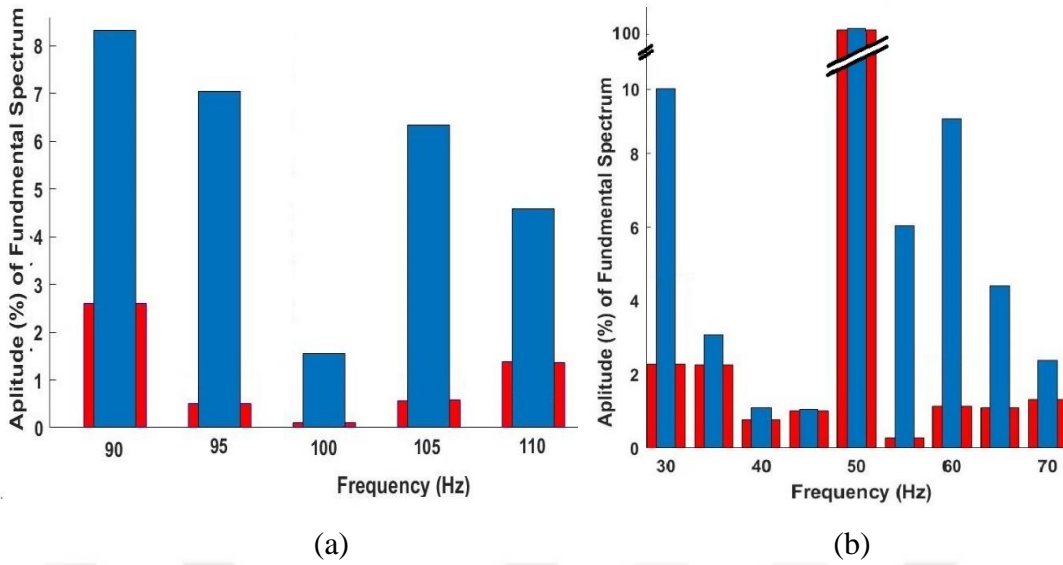


Figure 3.8. Comparison of the DFT spectrums of the original current Phase-A current waveform of 10 cycles (blue) and (a) that of waveform from which the components at 95Hz, 100Hz, and 105Hz obtained by MSRF+ES with optimal ES orders are subtracted (red); (b) that of waveform from which the components at 30Hz, 55Hz, 60Hz, and 65Hz obtained by MSRF+ES with optimal ES orders are subtracted (red), to simulate an APF operation

3.3. Results for Classification of PQ Events

During the train procedure of the MLCNN, 85% of the event data is used. In order to determine the number of epochs needed for accurate classification, accuracy and loss functions of the DIGITS platform is used. In Figure 3.8 (a), loss and accuracy functions versus epoch number is plotted for the train data. Learning rate is also provided by DIGITS up to epoch number 150 as given in Figure 3.8 (b). In terms of the learning rate, it is observed that epoch numbers 65 and 135 are critical, but increasing it more than 135 seems to be useless. It is also observed in Figure 3.8 (a) that when the epoch reaches 135, accuracy and loss remain approximately the same.

Figs. 3.9. and 3.10. show some of the classification results obtained by the trained system based on the test data, which is 15% of the whole PQ event data. Figure 3.9 shows sample interruption events with the classification predictions next to it. It is observed that although the event durations of interruption is completely different in events Figure 3.9 (a) and 3.9 (b), the classifications obtained by deep learning correspond to the correct one with 99.76% and 94.08%, respectively. Figure 3.10 shows other sample events from the test data classified. It is observed that the proposed classification is also successful in discriminating

dip events with different amplitudes and durations. Classification results of all the test data are compared with the labels assigned by the human expert and it is observed that 100% of the test data is classified correctly with the proposed deep learning-based PQ event classification algorithm. It is interesting to note that, images of the PQ events, but not the event waveforms themselves are used for classification. Thus, thanks to the processing speed and high accuracy of deep learning algorithms on images, both off-line and online classification of PQ events will be possible with the proposed PQ classification method.

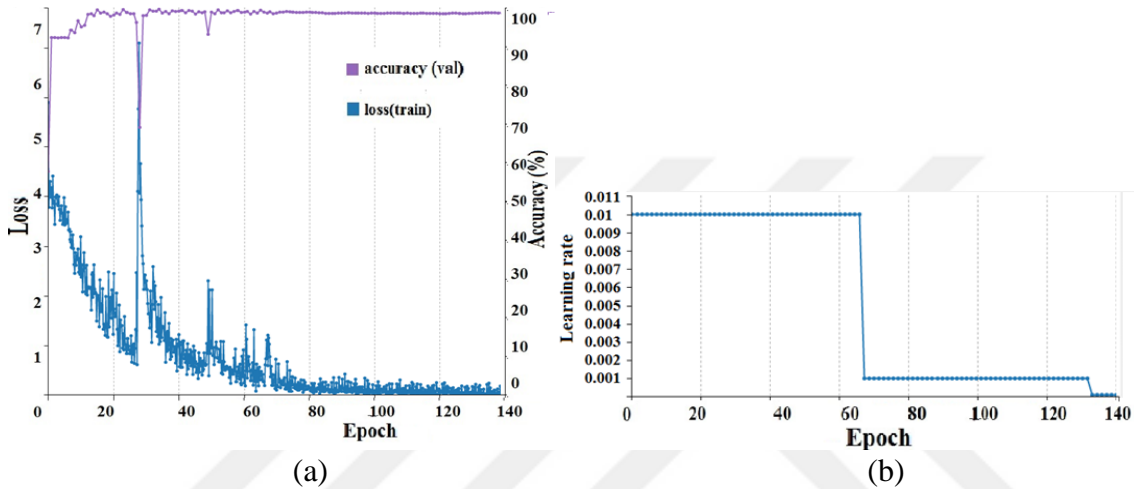
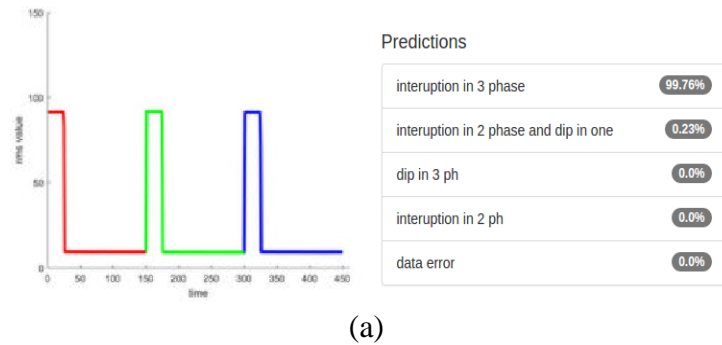


Figure 3.9. Loss and accuracy versus epoch number during the MLCNN training



(a) eventrgb2 Image Classification Model

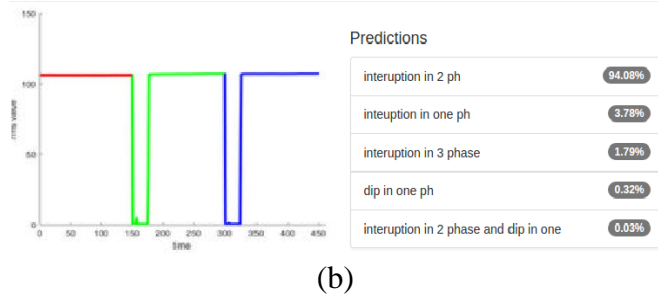
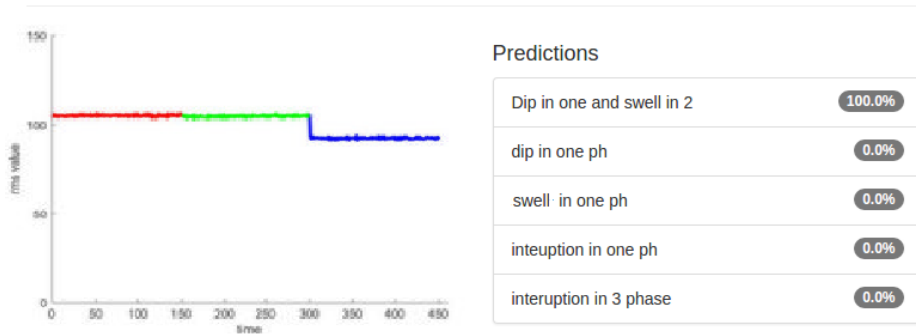


Figure 3.10. Examples of interruption event images out of the PQ event data used for test with the predicted event types using deep learning in DIGITS platform, (a) interruption in three phases, (b) interruption in two phases

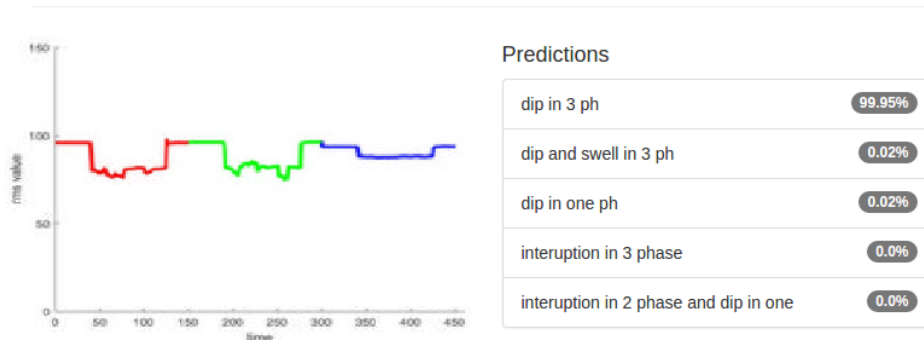
fast operation time of DL based algorithms, it can be concluded that the developed algorithm can be used to real-time and offline detection of PQ events.

eventrgb2 Image Classification Model



(a)

eventrgb2 Image Classification Model



(b)

Figure 3.11. Examples of dip and swell event images out of the PQ event data used for test with the predicted event types using deep learning in DIGITS platform, (a) long dip in one phase, (b) dip in three phases



4. CONCLUSION

In this section conclusions and discussions over the proposed methods described in the previous sections are presented. The aim of this thesis is to develop tools which will provide complementary solutions to develop a complete and smart power quality (PQ) monitoring system. Based on the survey carried out on the current literature on PQ analysis and commercial devices, the following needs can be listed at first sight:

- (i) fast and efficient light flicker computation: Flicker severity is computed over 10-min raw data of voltage, which is demanding in terms of both memory requirements and data processors,
- (ii) real-time harmonics and interharmonics computation: In cases of highly time-varying harmonics and interharmonics, it is important to be able to serve fast and accurate references to the applications such as active filters for a successful compensation,
- (iii) accurate PQ event classification: Automatic classification of PQ events is crucial for a smart grid to take actions automatically after the detection of any event.

Hence, new and novel methods have been proposed to solve the above-mentioned problems. The first method proposed is a new method for the evaluation of light flicker out of the root-mean-square (RMS) computations of voltage waveforms instead of using the whole 10-min raw data. According to the IEC and IEEE standards, light flicker computation is achieved on the raw data of the voltage waveforms. However, in many real world systems, since raw data storage is expensive and difficult, only RMS values of the voltage are stored for later analysis. This thesis proposes a new method to compute light flicker directly from RMS values of the voltage, which also comply with the IEC power quality standard, IEC 61000-4-30. It has been shown that the developed method reveals significantly satisfactory estimations of flicker sensation and severity values, obtained from the RMS strings of the voltage waveforms when compared with those obtained by the digital realization of the IEC flickermeter. It can be mentioned that this method provides an accurate, simple, and fast solution for the flicker computation, where raw data of the voltage waveforms are not available, but RMS values are present. The developed method is directly based on the current form of the IEC flickermeter, which includes the response of the incandescent lamps and the human eye response to the voltage fluctuations. Since the proposed method uses the response tables given in the IEC standard as explained in Section

3 of this thesis, if response to other types of lamps are included in the future versions of the IEC flickermeter, it can easily be adopted to the new lamp responses. Hence, the proposed method has the flexibility of considering the lamp type for any possible future versions of the IEC flickermeter. The method can be easily adopted by smart-grid applications, where fast and accurate flicker computation is required from RMS voltage waveforms, especially for generating control signals for the FACTS devices.

The second part of this thesis proposes the use of exponential smoothing (ES) together with the Multiple Synchronous Reference Frame (MSRF) analysis to estimate the EAF current harmonics and interharmonics, which are time-varying and stochastic due to the nature of the EAF operation. ES is a statistical technique used for detecting the data trend especially used in economics, which has been shown in this thesis to improve the amplitude and phase estimations of the time-varying harmonics and interharmonics, with minimized phase delay compared to other methods used previously for low-pass filtering in MSRF analysis. In order to achieve real-time processing of all EAF current harmonics and interharmonics to serve the needs of the controllers of the modern compensation systems such as active power filters (APF) for the automatic compensation of power system harmonics and interharmonics in smart grid applications, graphical processing unit (GPU) of NVIDIA (GEFORCE GTX 960 graphical processor) of the laptop computer is employed for the parallel processing of all harmonics and interharmonics. It has been shown using actual EAF current waveforms that real-time processing is possible to analyze all harmonics up to 50th and all interharmonics at 5Hz resolution. Moreover, active filtering of certain harmonics and interharmonics has been achieved in the simulation environment and it has been shown that successful real-time filtering of any harmonic and interharmonic component is possible with the proposed MSRF+ES method. It has to be mentioned that the proposed method helped to reduce the filtering delay of Kalman filter from 3ms approximately almost 1 ms. Hence the computation time of a single sample with the proposed method is reduced to 1 μ s, which gives the opportunity to make the system operating in real-time.

Finally, in the third part of the thesis, a power quality (PQ) event classification method using deep learning of the PQ event images is proposed. PQ events are defined as voltage sags, swells, and interruptions in the three phases of the electricity grid. Many methods for PQ event classification have been proposed in the literature; however, the proposed one is

the first one using the images of the PQ events instead of the voltage data vectors. The proposed method takes the advantage of the success of the deep-learning (DL) algorithms on image data. Therefore, the novelty of the proposed approach is that, images of the voltage waveforms of three phases of the power grid are classified with 100% accuracy, instead of classifying the sampled voltage data strings of the three phases. The *DIGITS* DL platform of *NVIDIA* is used for training and testing of the proposed method. Future work is planned to be increasing the number of train and test data with applying an automatic clustering algorithm for initial labeling of the train data. The proposed work is believed to serve the needs of the future smart grid applications, which are fast and automatic analysis of the electricity grid and taking automatic countermeasures against potential PQ events. Thus, thanks to the processing speed and high accuracy of deep learning algorithms on images, both off-line and online classification of PQ events will be possible with the proposed PQ classification method.

As future work, all three proposed methods can be used to upgrade an existing PQ monitoring system, which is developed suitable for future upgrades, such as the PQ^+ monitoring system developed through the National Power Quality Project of Turkey [55], to make it a smart-grid monitoring system of the future.



REFERENCES

1. IEC Standard 61000-4-30, (2008). *Electromagnetic Compatibility (EMC) – Part 4-30: Testing and Measurement Techniques – Power Quality Measurement Methods*.
2. IEC Standard 61000-4-15, (2003). Testing and measurement techniques – Section 15: Flickermeter – Functional and design specifications.
3. Wu, C. J., Chen and Y.J., (2006). A Novel Algorithm for Precise Voltage Flicker Calculation by Using Instantaneous Voltage Vector. *IEEE Trans. Power Delivery*, 3(21), 1541-48.
4. Hernandez A., Mayordomo, J. G. R., Asensi, and Beites, L.F., (2003). A new frequency approach for flicker evaluation of arc furnaces. *IEEE Trans. Power Delivery*, 2(18), 631–638.
5. Wu, C.J., Fu, T.H., (2003). Effective voltage flicker calculation algorithm using indirect demodulation method. *IET Generation, Transmission & Distribution*. 150, (4) 493 - 500.
6. Balouji, E., Salor, O., (2016). Digital realisation of the IEC flickermeter using root mean square of the voltage waveform, *IET Generation, Transmission & Distribution*, 7(10), 1663 – 1670.
7. Kose, N., Salor, O., (2009). New spectral decomposition based approach for flicker evaluation of electric arc furnaces, *IET Generation, Transmission & Distribution*, 4(10), 393 - 411.
8. Cho, S., Park C. H., Han J., and Jang, G., (2012). A Waveform Distortion Evaluation Method Based on a Simple Half-Cycle RMS Calculation. *IEEE Transaction Power Delivery*, 3(27).
9. Kose, N., Salor, O., Leblebicioglu, K., (2009). Kalman filtering based approach for light flicker evaluation of power systems. *IET Generation, Transmission & Distribution*, 1(5), 57 – 69.
10. Hernández, A., Mayordomo, J., Asensi, G., Luis, R., Beites, F., (2003). A New Frequency Domain Approach for Flicker Evaluation of Arc Furnaces. *IEEE Trans On Power Delivery*, 2(18), 631 - 638.
11. Yang, X., Kratz, M., (2007). *Power System Flicker Analysis and Numeric Flicker Meter Emulation*. IEEE PES Conference Power Tech, 1-5.
12. Gutierrez, J., J. Ruiz, U. Irusta, S. Ruiz de Gauna, 2008., A New Alternative for the Input-Voltage Adaptor of the IEC Flickermeter. *IEEE Trans on Instrumentation and Measurement*, 5(57) 923 - 930.
13. Wang, S., Michael J., (2004). Incandescent Lamp Flicker Mitigation and Measurement. *IEEE Trans on Instrumentation and Measurement*, 4(53) 1028 - 1034.
14. Tayjasanant, T., Wang, W., Li, C., and Xu, W., (2005). Interharmonic-Flicker Curves. *IEEE Trans on Power Delivery*, 2(20).

15. Demirci, T., Kalaycioglu A., Kucuk, D., Salor, O., Guder, M., Pakhuylu, S., Atalık, T., Inan, T., Cadirci, I., Akkaya, Y., Bilgen, S., Ermis M., (2010). Nationwide Real-Time Monitoring System for Electrical Quantities and Power Quality of the Electricity Transmission System. ***IET Gener. Transm. Distrib***, 5(5), 540 - 550.
16. Atalik, T., Cadirci, I., Demirci, T., Ermis, M., Inan, T., Kalaycioglu, A., Salor, Ö., (2014). Multipurpose Platform for Power System Monitoring and Analysis with Sample Grid Applications. ***IEEE Trans on Instrumentation and Measurement***, 3(63), 566 - 582.
17. Salor, O., Gultekin, B., Buhan, S., Boyrazoglu, B., Inan, T., Atalik, T., Acik, A., Terciyanli A., Unsar, Altintas, O., Akkaya, Y., Ozdemirci, E., Cadirci, I., and Ermis, M., (2010). Electrical power quality of iron and steel industry in Turkey. ***IEEE Transactions On Industry Application***, 1(46), 60–80.
18. Yilmaz I., and Salor, O., (2012). Field-data-based modeling of medium-frequency induction melting furnaces for power quality studies, ***IEEE Transactions On Industry Application***, 4(48), 1215–1224.
19. Srdic, S., Nedeljkovic, M., and Vukosavic, S., (2016). Fast and Robust Predictive Current Controller for Flicker Reduction in DC Arc Furnaces. ***IEEE Transaction on Industrial Electronics***, 7(63) 4628 - 4640.
20. Asiminoaei, L., Blaabjerg, F., and Hansen, S., (2007). Detection is the key—Harmonic detection methods for active power filter applications, ***IEEE Transactions On Industry Application***, 4(13), 22–33.
21. Chen, C.I. and Chen, Y. C., (2014). Comparative Study of Harmonic and Interharmonic Estimation Methods for Stationary and Time-Varying Signals. ***IEEE Transactions on Industrial Electronics***, 1(6), 397-404.
22. Leonowicz, Z., Lobos, T. and Rezmer, J., (2003). Advanced Spectrum Estimation Methods for Signal Analysis in Power Electronics. ***IEEE Transactions on Industrial Electronics***, 3(50) 514 - 519.
23. Uz-Logoglu, E., Salor, O. and Ermis, M., (2016). Online characterization of interharmonics and harmonics of AC electric arc furnaces by multiple synchronous reference frame analysis. ***IEEE Trans. Industry Appl.***, 52(3), 2673–2683.
24. Gary W., Chen C., and Liang, Q. W., (2009). A Two-Stage ADALINE for Harmonics and Interharmonics Measurement. ***IEEE Transactions on Industrial Electronics***, 6(56), 2220 – 2228.
25. Gary W. and et al, (2010). On Real-Time Simulation for Harmonic and Flicker Assessment of an Industrial System with Bulk Nonlinear Loads. ***IEEE Trans. Industrial Electronics***, 9(57).
26. Chen, C., and Gary W. C., (2010). Virtual Instrumentation and Educational Platform for Time-Varying Harmonic and Interharmonic Detection, ***IEEE Transactions on Industrial Electronics***, 10(57).

27. Gunlu E., and Salor, O., (2014). *Harmonic and interharmonic analysis of power signal using synthetic resampling*. In Proc. IEEE 22nd Signal Process. Commun. Appl. Conf. (SIU'14), 750–753.
28. Chen, C., and Chang, W., (2013). An Efficient Prony-Based Solution Procedure for Tracking of Power System Voltage Variations. *IEEE Transactions on Industrial Electronics*, 7(60). 2681 - 2688
29. Yacamini, R., (1996). Power system harmonics: Part 4 interharmonics. *Power Engineering Journal*, 10, 183–193.
30. Zhezhelenko I., and Sayenko, Y., (2000). *Analysis methods of interharmonics investigations in power systems*. in Proc. IEEE 9th Int. Conf. Harmon. Qual. Power (ICHQP'2000), 61–63.
31. Kose N. and Salor, O., (2009). New spectral decomposition-based approach for flicker evaluation of electric arc furnaces. *IET Generation Transmiss. Distribution*, 4(3), 393–411.
32. Salor, O., (2009). Spectral correction-based method for interharmonics analysis of power signals with fundamental frequency deviation. *Journal of Electric Power Systems Res.*, 79, 1025–1031.
33. Testa, A., Akram, M. F. and Burch. R., (2007). Interharmonics: Theory and modeling, , *IEEE Trans. Power Del.*, 22(4), 2335–2348.
34. Hui, J. Yang, H. Xu, W. and Liu, Y., (2012) A method to improve the interharmonic grouping scheme adopted by IEC standard 61000-4-7, *IEEE Transaction on Power Delivery*, 27(2), 971–979.
35. Golestan, S., Monfared, M. and Freijedo, F. D., (2013). Design-oriented study of advanced synchronous reference frame phase-locked loops. *IEEE Transaction on Power Electronins*, 2(28), 765–778.
36. Sun, S., Ben, H., meng, T., and Zhang, J., (2014). *A new PLL based on fast positive and negative-sequence decomposition algorithm with matrix operation under distorted grid conditions*, in Proc. IEEE Int. Power Electron. Conf. (IPEC-Hiroshima 2014-ECCE-ASIA), 3213–3217
37. S., Golestan, J., Guerrero, and Vasquez. J., (2016). Three-phase PLLs: A review of recent advances. *IEEE Transaction on Power Electronins*, 3(32).
38. Baoquan, L., Zhuo, F., Zhu, Y., Yi, H. and Weng, F., (2015). A three-phase PLL algorithm based on signal reforming under distorted grid conditions, *IEEE Transaction on Power Electronins*, 9(30), 5272–5283.
39. Kose, N. Salor, O. and Leblebicioglu, K., (2011). Kalman filtering based approach for light flicker evaluation of power systems. *IET Generation, Transmission & Distribution*, 5(1), 57-69.
40. Robles, E. Pou, J. Ceballos, S. et. al, (2011). Frequency-adaptive stationary-reference-frame grid voltage sequence detector for distributed generation systems. *IEEE Transaction on Industry Electronics*, 9(58), 4275–4287.

41. Moreno, V., Liserre, M., Pigazo, A. and et al, (2007). A comparative analysis of real-time algorithms for power signal decomposition in multiple synchronous reference frames. ***IEEE Transactions on Power Electronics***, 22(4), 1280–1289.
42. Xiao, P., Corzine, K. A. and Venayagamoorthy, G. K., (2008). Multiple reference frame-based control of three-phase PWM boost rectifiers under unbalanced and distorted input conditions. ***IEEE Transaction on Power Electronics***, 4(23), 2006–2017.
43. Loh, P. C., Tang, Y., Blaabjerg, F. and Wang, P., (2011). Mixed-frame and stationary-frame repetitive control schemes for compensating typical load and grid harmonics. ***IET Power Electronics***, 2(4) 218–226.
44. Chen, G., Zhu, M. and Cai, X., (2013). Medium-voltage level dynamic voltage restorer compensation strategy by positive- and negative-sequence extractions in multiple reference frames. ***IET Power Electronics***, 7(7), 1747–1758.
45. Chiyoung L., Kim, S., W., Yoo, C., (2012). VADI: GPU Virtualization for an Automotive Platform. ***IEEE Transaction on Industrial Informatics***, 1(12), 277 - 290.
46. Roberge, V., Tarbouchi, M., and Labonté, G., (2015). Parallel Algorithm on Graphics Processing Unit for Harmonic Minimization in Multilevel Inverters, ***IEEE Transactions on Industrial Informatics***, 3(11), 700 - 707.
47. Daloukas, K., Evmorfopoulos, N., Tsompanopoulou, P., et.al. (2016). Parallel Fast Transform-Based Preconditioners for Large-Scale Power Grid Analysis on Graphics Processing Units (GPUs). ***IEEE Transaction on Computer-Aided Design of Integrated Circuits And Systems***, 10(35), 1653 - 1666.
48. Brown, R. G., (1956). Exponential Smoothing for Predicting Demand. Cambridge, Massachusetts: Arthur D. Little Inc.
49. Holt, C., (2004). Forecasting trends and seasonal by exponentially weighting averages. ***International Journal of Forecasting***, 1(20), 5-10.
50. Brown, R. G., (1963). Smoothing Forecasting and Prediction of Discrete Time Series, Englewood Cliffs, NJ: Prentice-Hall, 1963.
51. Taylor J.W., (2012). Short-term load forecasting with exponentially weighted methods. ***IEEE Transactions on Power Systems***, 1(27), 458-464.
52. Che, S., Jremy, Sheaffer, W., Skadron K. and Lach J., (2008). Accelerating Compute-Intensive Applications with GPUs and FPGAs. Symposium on Application Specific Processors, 2008.
53. Atalik, T., Çadirci, I., Demirci, T., Ermis, M., Inan, T., Kalaycioglu, A. and Salor, Ö., (2014). Multipurpose Platform for Power System Monitoring and Analysis with Sample Grid Applications. ***IEEE Transaction on Instrument and Measurements***, 3(63), 566 - 582.
54. Electromagnetic Compatibility (EMC)—Part 4–7: *Testing and Measurement Techniques—General Guide on Harmonics and Interharmonics Measurements and Instrumentation, for Power Supply Systems and Equipment Connected Thereto*, IEC Standard 61000-4-7, 2005.

55. Demirci, T., Kalaycioglu, A., Kucuk D., et al, (2011). Nationwide real-time monitoring system for electrical quantities and power quality of the electricity transmission system, ***IET Generation, Transmission and Distribution***, 5(5), 540-550.
56. Atalik, T., Cadirci, I., Demirci, T., Ermis, M., Inan, Kalaycioglu, T., and Salor, O., (2014). Multipurpose Platform for Power System Monitoring and Analysis with Sample Grid Applications. ***IEEE Transaction on Instrumentation and Measurement***, 3(63).
57. Guder, M., Salor, O., Cadirci, I., Ozkan, B. and Altintas, E., (2015). Data Mining Framework for Power Quality Event Characterization of Iron and Steel Plants, ***IEEE Transactions On Industry Applications***, 4(5).
58. Balouji, E., and Salor, O., (2014). Eigen-Analysis Based Power Quality Event Data Clustering and Classification. IEEE PES Innovative Smart Grid Technologies, Europe,
59. Balouji, E., (2014). *Automatic clustering of power quality events using pattern recognition techniques for smart grid applications*. M.Sc. Thesis, Gazi University.
60. Eris, H. and Demir, Y., (2012). Automatic classification of power quality events and disturbances using wavelet transform and support vector machines. ***IET Generation, Transmission & Distribution***, 6(10), 968 - 976.
61. Biswal, B., Mishra S. and Jalaja, R., (2014). Automatic Classification of Power Quality Events Using Balanced Neural Tree. ***IEEE Transactions On Industrial Electronics***, 1(61), 521 - 530.
62. Shukla, S., Mishra, S. and Singh, B., (2014). Power Quality Event Classification Under Noisy Conditions Using EMD-Based De-Noising Techniques. ***IEEE Transactions On Industrial Informatics***, 2(10), 1044 - 1054.
63. Kumar, R. Singh, B., Shahani, D. T., Chandra, A. and Al-Haddad, K., (2015). recognition of power-quality disturbances using S-transform-based ANN classifier and rule-based decision tree. ***IEEE Transactions On Industry Applications***, 2(51). 1249 – 1258.
64. Naderian S. and Salemnia A., (2016). Method for classification of PQ events based on discrete Gabor transform with FIR window and T2FK-based SVM and its experimental verification. ***IET Generation, Transmission & Distribution***, 1(11), 133 – 141.
65. Balouji E. and Salor, O., (2017). Classification of power quality events using DL on event images, in proc. IEEE Int. IPRIA conf., 216-221.
66. Szegedy, C., Liu, W., Jia, Y., Sermanet, P., Reed, S., Anguelov, D., Erhan, D., Vanhoucke, V., Rabinovich, A., Hill, C., Arbor A., Leap, M., (2015). Going Deeper with Convolutions. IEEE Conference on Computer Vision and Pattern Recognition (CVPR).
67. Krizhevsky, A., Sutskever, I. and Hinton, G., (2012). *Image net classification with deep convolutional neural networks*. Advances in neural information processing systems, 1097-1105.
68. LeCun, Y., Bottou, L., Bengio, Y., and Haffner, P., (1998). Gradient-based learning applied document recognition. ***Proceeding of IEEE***, 2278 - 2324.

69. Silver, D., and et al, (2017). Mastering the game of go without human knowledge. *Springer Nature*, 550.
70. Ranjan R. and et al, (2018). Deep Learning for Understanding Faces: Machines May Be Just as Good, or Better, than Humans. *IEEE Signal Processing Magazine*, 1(35) 66 - 83.
71. Ballas, N., Li, Y., Pal C. and Courville, A., (2016). Delving deeper into convolutional network for learning video representations. in proc. ICLR, 2016.
72. Bartl, M., (2018). YouTube channels, uploads and views: A statistical analysis of the past 10 years. *The International Journal of Research into New Media Technologies*, 24(1), 16–32.



CURRICULUM VITAE

Personal Information

Surname, Name : BALOUJI Ebrahim
 Nationality : T.C. 9914349800
 Date and Place of Birth : 25.06.1985, Marand
 Marital status : Single
 Phone number : +46 721705218
 e-mail : balouji@gmail.com



Education

Degree	School/ Program	Graduation Date
PhD	Gazi University / Electrical Electronics Eng	Ongoing
MSc	Gazi University / Electrical Electronics Eng	2015
Undergraduate	Gazi University / Electrical Electronics Eng	2010
High School	Bahman Shamloo	2006

Employment History

Date	Work Place	Occupation
2018	Sweden, Chalmers university of Technology	Research Assistant

Foreign Language

English

Publications

- Balouji, E., Salor, O. and Ermis, M. (2018). *Exponential smoothing of multiple reference frame components with gpus for real-time detection of time-varying harmonics and interharmonics of EAF currents*. IEEE Transaction on Industry Applications.
- Balouji, E. and Salor, O. (2016). *Digital realization of the iec flickermeter using root mean square of the voltage waveform*. IET Generation, Transmission, and Distribution.

3. Balouji, E., Irene, Y., Gu, H., Math, H., Bollen, J., Bagheri, A. and Nazari, M. (2018). *LSTM-based deep learning method with application to voltage dip classification*. International Conference Harmonics and Quality of Power ICHQP, Ljubljana Slovenia.
3. Balouji, E. and Salor, O. (2017). *Comparison of MAF and Kalman Filter Performances in Multiple Synchronous Reference Frame Analysis to Determine Harmonics and Interharmonics of EAF currents*. International Conference on ENERGY and ENVIRONMENT CIEM, Romania.
4. Balouji, E., Salor, O. and Ermis, M. (2017). *Exponential smoothing of multiple reference frame components with GPUs for real-time detection of time-varying harmonics and interharmonics of EAF currents*. 2017 IEEE Industry Applications Society Annual Meeting.
5. Balouji, E. Salor, O. (2017). *Power quality event classification using deep learning*, IEEE, IPRIA 2017, Shahr Kord, Iran.
6. Celik, M. E. and Balouji, E. (2017). *Characterization of individual retinal ganglion cell responses using K-means clustering method*. International Artificial Intelligence and Data Processing Symposium IDAP Malatya, Turkey.
7. Kashtiban, M. G. and Balouji, E. (2016). *Analyzing and implementation of a ZVT boost converter used in PV applications*. IEEE PES Innovative Smart Grid Technologies Conference Europe ISGT Ljubljana Slovenia.
8. Balouji, E. and Salor, O. (2015). *Assessment of RMS computation in terms of power quality event detection*. IEEE SIU, Malatya, Turkey.
9. Balouji, E. and Salor, O. (2015). *Light flicker evaluation using root mean square voltage waveforms*. IEEE 56th international Conference on Power Engineering, RTUCON.
10. Balouji, E. and Salor, O. (2014). *Eigen-analysis based power quality event data clustering and classification*. IEEE PES Innovative Smart Grid Technologies, Istanbul, Turkey.
11. Bagheri, A., Gu, I., Bollen, M. and Balouji, E. (2018). *A robust transform-domain deep convolutional network for voltage dip classification*. IEEE Transaction on Power Delivery.

Hobbies

Reading, running, music,



GAZİ GELECEKTİR..

